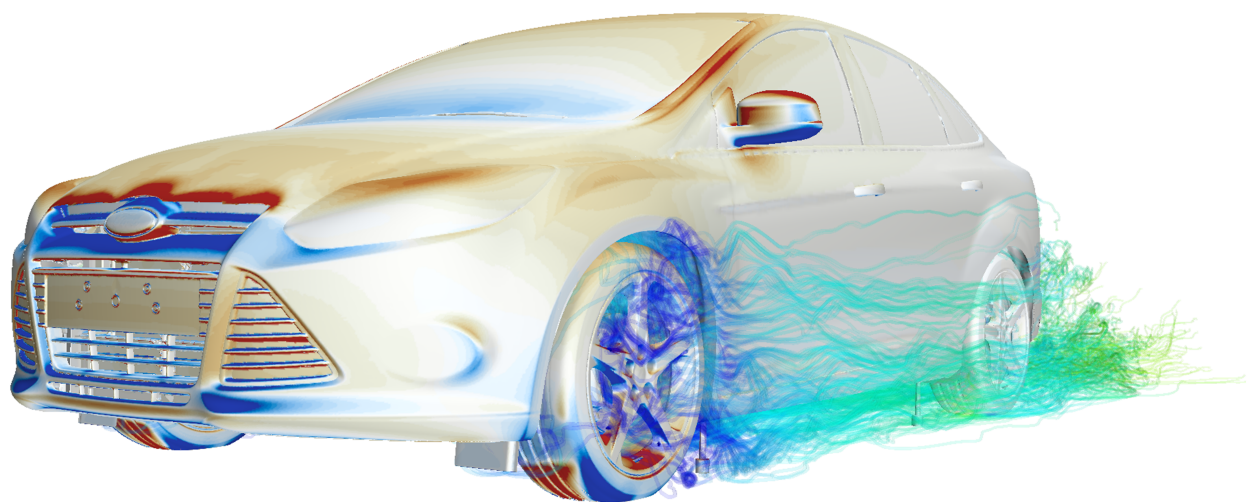




# CHALMERS

---



## **Numerical Analysis of Cooling Drag and Front Lift Interaction on a Ford Focus**

Master's thesis in Applied Mechanics

MAGNUS URQUHART



MASTER'S THESIS IN APPLIED MECHANICS

Numerical Analysis of Cooling Drag and Front Lift Interaction on a Ford  
Focus

MAGNUS URQUHART

Department of Applied Mechanics  
Division of Vehicle Engineering and Autonomous Systems  
CHALMERS UNIVERSITY OF TECHNOLOGY

Göteborg, Sweden 2016

Numerical Analysis of Cooling Drag and Front Lift Interaction on a Ford Focus  
MAGNUS URQUHART

© MAGNUS URQUHART, 2016

Master's thesis 2016:76  
ISSN 1652-8557  
Department of Applied Mechanics  
Division of Vehicle Engineering and Autonomous Systems  
Chalmers University of Technology  
SE-412 96 Göteborg  
Sweden  
Telephone: +46 (0)31-772 1000

Cover:

Illustration of surface coloured by  $C_{l_{front}}$  with streamlines exiting the radiator coloured by  $C_p$

Chalmers Reproservice  
Göteborg, Sweden 2016

Numerical Analysis of Cooling Drag and Front Lift Interaction on a Ford Focus  
Master's thesis in Applied Mechanics  
MAGNUS URQUHART  
Department of Applied Mechanics  
Division of Vehicle Engineering and Autonomous Systems  
Chalmers University of Technology

## ABSTRACT

Changes in front lift have been observed by Ford Motor Company and other OEMs (original equipment manufacturers) when varying the amount of cooling flow. This flow phenomena is not yet fully understood, further the predictions made by CFD (Computational Fluid Dynamics) have shown to underpredict front lift compared to experiments.

The thesis work aims to increase understanding of how cooling flow effects front lift as well as investigate the accuracy of unsteady FVM (Finite Volume Method) CFD simulations. The FVM simulation results are compared to wind tunnel tests and results from another solver using the LBM (Lattice Boltzmann Method) with focus on cooling flow and predicted trends between vehicle configurations. Drag is of larger interest than lift when optimizing road vehicle aerodynamics, however, front lift and the overall lift balance of a vehicle effects high speed handling with effects apparent at speeds over 80 km/h.

The results show that front lift is increased due to cooling flow and that the largest changes in cooling drag and front lift are located at the front part of the car. The front lift increase due to cooling flow is due to two components; the lift component and the drag component which changes the front and rear lift distribution. The accuracy and trend-predicting capability of the FVM and LBM simulations is similar for the numerical setup used in this thesis. The numerical solvers were often closer to each other than to experimental values.

Keywords: Cooling flow, Front lift, Cooling drag, CFD, Ford, Focus, Unsteady, IDDES, FVM, LBM



## PREFACE

In this report unsteady FVM (Finite Volume Method) CFD simulations are performed to investigate the effects of cooling flow on front lift. The FVM CFD results are also compared to previously existing CFD results from another solver using the LBM (Lattice Boltzmann Method) to compare absolute accuracy as well as capability to predict trends. The work is done on three vehicle configurations at three conditions; closed cooling, open cooling and closed AGS (active grill shutter), resulting in a total of nine simulations. By increasing the understanding of how the cooling flow effects front lift it is easier to make modelling choices for simulations to better capture front lift as well as achieve front lift targets during the design phase of a vehicle. The project is carried out at the department of Applied Mechanics, division of Vehicle Engineering and Autonomous Systems, Chalmers, together with Ford Motor Company Cologne.

I would like to thank my examiner Associate Professor Simone Sebben at the department of Applied Mechanics, division of Vehicle Engineering and Autonomous Systems, Chalmers, and colleagues Teddy Hobeika, Emil Ljungskog and Sabine Bonitz for their continuous support and interesting discussions throughout the project.

I would also like to thank Dr Burkhard Hupertz at Ford Motor Company Cologne for the thesis opportunity and colleagues Christian Wenigwieser, Lothar Krueger and Dr Jan Westphalen for the introduction at Ford Motor Company Cologne as well as all the support, provided results and time invested throughout the project.



## NOMENCLATURE

CFD	Computational Fluid Dynamics
FVM	Finite Volume Method
LBM	Lattice-Boltzmann Method
OEM	Original Equipment Manufacturer
AGS	Active Grille Shutter
LES	Large Eddy Simulation
RANS	Reynolds-Averaged Navier-Stokes
IDDES	Improved Delayed Detached Eddy Simulation
CoP	Centre of pressure
SST	Shear Stress Transport
$Cl$	Coefficient of Lift
$Cd$	Coefficient of Drag
$Cl_f$	Coefficient of Front Lift
$Cp$	Coefficient of Pressure
$Cm_{rear}$	Coefficient of Moment around rear wheels
$\Delta Cd$	Cooling drag coefficient
$\Delta Cl$	Cooling lift coefficient
$\Delta Cl_f$	Cooling front lift coefficient
$C\dot{m}$	Mass flow coefficient
$Re$	Reynolds number
$\varepsilon$	Turbulent dissipation [ $m^2/s^3$ ]
$\omega$	Specific dissipation rate [ $1/s$ ]
$k$	Turbulent kinetic energy [ $m^2/s^2$ ]
$\nu$	Kinematic viscosity [ $m^2/s$ ]
$\nu_t$	Eddy viscosity [ $m^2/s$ ]
$\mu$	Viscosity [ $kg/(m \cdot s)$ ]
$\rho$	Density [ $kg/m^3$ ]
$\infty$	Subscript denoting free-stream values
$V$	Velocity in wind direction [ $m/s$ ]
$y^+$	Dimensionless first cell centre height
$s^+$	Dimensionless first cell streamwise length
$l^+$	Dimensionless first cell spanwise length
$\tilde{\Phi}$	Time-averaged quantity
$\bar{\Phi}$	Volume-averaged quantity



# CONTENTS

<b>Abstract</b>	<b>i</b>
<b>Preface</b>	<b>iii</b>
<b>Nomenclature</b>	<b>v</b>
<b>Contents</b>	<b>vii</b>
<b>1 Introduction</b>	<b>1</b>
1.1 Background . . . . .	1
1.2 Purpose . . . . .	1
1.3 Limitations . . . . .	2
<b>2 Theory</b>	<b>3</b>
2.1 Non-dimensional quantities . . . . .	3
2.1.1 Force coefficients . . . . .	3
2.1.2 Front lift . . . . .	3
2.1.3 Reynolds number . . . . .	3
2.1.4 Pressure coefficient . . . . .	4
2.1.5 Cell size . . . . .	4
2.2 Governing equations . . . . .	4
2.3 Turbulence modelling . . . . .	4
2.3.1 LES . . . . .	5
2.3.2 Unsteady-RANS . . . . .	5
2.3.3 SST $k - \omega$ . . . . .	6
2.3.4 DES . . . . .	7
2.3.5 DDES . . . . .	7
2.3.6 IDDES . . . . .	7
2.4 Wall treatment . . . . .	8
2.5 Porous media . . . . .	8
<b>3 Method</b>	<b>9</b>
3.1 Configurations . . . . .	9
3.1.1 Cooling flow . . . . .	9
3.1.2 $\Delta$ Cooling flow between configurations . . . . .	10
3.2 Wind tunnel . . . . .	10
3.3 Simulation . . . . .	10
3.3.1 Geometry . . . . .	10
3.3.2 Mesh . . . . .	11
3.3.3 Simulation setup . . . . .	13
3.4 Post-processing . . . . .	15
3.4.1 Accumulated 1D . . . . .	15
3.4.2 Integrated 2D . . . . .	16
3.4.3 Mass flow . . . . .	16
<b>4 Results</b>	<b>17</b>
4.1 Wind tunnel and numerical comparison . . . . .	17
4.1.1 Total values . . . . .	17
4.1.2 Pressure probes . . . . .	19
4.2 Front lift and cooling drag interaction . . . . .	27
4.2.1 Accumulated 1D . . . . .	27
4.2.2 Integrated 2D . . . . .	28
4.2.3 Mass flow . . . . .	32

<b>5 Discussion</b>	<b>33</b>
5.1 Results	33
5.2 Influencing factors	33
5.2.1 Wind tunnel	33
5.2.2 Probe location	34
5.2.3 Geometry	34
5.3 Future work	35
5.3.1 Numerical accuracy	35
5.3.2 Front lift and cooling flow interaction	35
<b>6 Conclusions</b>	<b>36</b>
<b>References</b>	<b>37</b>

## Figures

3.1 Vehicle configurations	9
3.2 Vehicle operating conditions	9
3.3 CFD and Pinifarina wind tunnel	10
3.4 Taped geometry	11
3.5 Surface mesh generated from the different meshing operations in STAR-CCM+	12
3.6 Pinifarina wind tunnel with Ford Focus	12
3.7 Volume mesh at the centerline	12
3.8 IDDES Blending factor - Top view	13
3.9 Simulation wind tunnel	14
3.10 Accumulated 1D plot	15
3.11 Integrated 2D plot	16
3.12 Control planes used to measure mass flow around the vehicle	16
4.1 $Cd$ for configuration A, B and C	17
4.2 $Cl_f$ for configuration A, B and C	18
4.3 Pressure probe locations - Centerline and Engine bay	19
4.4 Pressure probe locations - Hood and Front bumper	19
4.5 Centerline probe - Configuration A, Open and Closed cooling	20
4.6 Centerline probe - $\Delta Cp_A$	20
4.7 Centerline probe - $\Delta \Delta Cp_{B-A}$	21
4.8 Engine bay probe - Configuration A, Open and Closed cooling	22
4.9 Engine bay probe - Configuration A, AGS Closed	22
4.10 Hood probes - Configuration A	23
4.11 Hood probes - Configuration A, Normalized by Wind Tunnel results	24
4.12 Front bumper probes - Configuration A	25
4.13 Front bumper probes - Configuration A, Normalized by Wind Tunnel results	26
4.14 Accumulated 1D - Open, Closed and $\Delta$ cooling for configuration A	27
4.15 Accumulated 1D - Open, Closed and $\Delta$ cooling for configuration B	27
4.16 Integrated 2D - Open cooling for configuration A	28
4.17 Integrated 2D - Delta cooling for configuration A	29
4.18 Integrated 2D - Delta front lift of components for configuration A	30
4.19 Integrated 2D - Delta delta front lift and drag	31
4.20 Cooling mass flow change - Rims and Control planes	32
4.21 Cooling mass - Radiator	32
5.1 Hood pressure and mesh	34
5.2 Closed cooling - Virtual vs real	34

# Tables

3.1	CFD Settings . . . . .	13
4.1	Force change (in counts) from 0.1 $C_p$ increase . . . . .	19



# 1 Introduction

A possible interaction between front lift and cooling drag has been observed by Ford Motor Company, where front lift is increased, similarly to drag, when there is cooling flow. Drag is of big importance for vehicle manufacturers when considering the aerodynamic properties of a vehicle in order to reduce fuel consumption and emissions. However, the overall lift and lift balance of a vehicle effects handling characteristics such as lane change manoeuvrability at high speeds with apparent effects at speeds over 80 km/h [1]. This thesis work aims to investigate how cooling flow effects front lift for different vehicle configurations. The accuracy and predictive capability of the FVM (Finite Volume Method) CFD (Computational Fluid Dynamics) simulations that are run is also investigated. The work is done on a Ford Focus four door saloon modified to have a smooth underbody in three different configurations, power train shield off, exhaust cover off and exhaust cover on. Each configuration is run at three operating conditions; open cooling, blanked cooling and with the active grill shutter fully closed resulting in a total of nine separate simulations. It is important to note that the vehicle with the different underbody configurations is only used for aerodynamic investigation and does not represent a production vehicle from Ford. Wind tunnel results from Pinifarina and CFD results from a LBM (Lattice-Boltzmann Method) solver are used to compare the accuracy and trend-predicting capability of the solvers.

## 1.1 Background

Computational Fluid Dynamics is used by OEMs (Original Equipment Manufacturers) as a tool to aid in design and understanding of vehicle aerodynamics together with wind tunnel measurements. CFD is gaining an increased importance in aerodynamic vehicle design as it is possible to optimise aerodynamic performance without the need of producing a physical model for wind tunnel tests, resulting in reduced lead times and cost. Ford have found that the accuracy and predictive capability of CFD, when comparing to wind tunnel results, was lacking in absolute accuracy as well as the predicted trends between configurations when investigating cooling flow. For the Ford Focus saloon car used in this thesis it was found that front lift is underpredicted by CFD (~40-60 counts) while drag is matching closer to wind tunnel results, (within ~10 counts) depending on configuration. Other OEMs have similarly found underpredictions in front lift when comparing CFD to wind tunnel results [2, 3].

Because of the importance of drag when considering the aerodynamic properties of a road vehicle the aerodynamic lift is often only mentioned as a side note in investigations on aerodynamic drag. The effects of cooling flow on drag has been documented on several occasions however the effects of cooling flow on lift and lift distribution is not as widely documented and remains an open field of research. According to Kremheller it was found that front lift decreased by 20% when reducing the cooling flow with an active grille shutter. However, the cause of the front lift change was not mentioned. [4] From wind tunnel testing Ford also found that the cooling flow increased front lift (~40-50 counts) depending on vehicle configuration. Work by Kuthada and Wiedemann show a similar increase in front lift when opening the cooling however the cause of the increase is not mentioned. [5]

## 1.2 Purpose

The thesis work presented has two main objectives, increasing the understanding on how front lift is effected by cooling flow; and evaluating the accuracy and trend-predicting capability of FVM CFD simulations. The accuracy and trend-predicting capability of the FVM CFD simulations is compared to results from a LBM-based solver and wind tunnel test. Special focus is put on how the FVM solver predicts the trends between vehicle configurations for open and closed cooling in order to evaluate the validity of the solver for cooling flow optimisation.

Increasing the understanding of the flow physics of cooling flow and investigating a possible interaction between cooling drag and cooling lift, can aid in aerodynamic design of road vehicles with beneficial effects on both drag and lift. Furthermore increasing the understanding of the flow physics can aid in the modelling choices made for CFD simulations that focus on cooling flow.

### 1.3 Limitations

This Master's Thesis is conducted by one person with a time limit of 20 weeks. The LBM simulation results will only be used for accuracy comparison with the FVM simulations; the simulation setup, theory and method for the LBM simulations will not be presented. If the reader is interested, a brief overview of the Lattice Boltzmann method is presented in "The Lattice-Boltzmann Method: An Alternative to LES for Complex Aerodynamic and Aeroacoustic Simulations in the Aerospace Industry" [6]. Since the work is done for one vehicle in three configurations at three operating conditions the results only give an indication of the predictive capability of FVM simulations using the setup presented in the Method chapter. Similarly the conclusions draw and the effect cooling flow has on front lift might not transfer well to other vehicles. The computational cost is limited so that the simulations can be run within reasonable time.

## 2 Theory

The simulations performed in this thesis work relies on solving the governing equations for viscous fluid flow on a mesh comprised of finite volumes. The governing equations and main ideas behind the RANS (Reynolds-Averaged Navier-Stokes)-LES (Large Eddy Simulation) SST (Shear Stress Transport)  $k - \omega$  IDDES (Improved Delayed Detached Eddy Simulation) turbulence model will be presented in this chapter as well as non-dimensional quantities used in post-processing and simulation setup.

### 2.1 Non-dimensional quantities

Non-dimensional quantities are often used in order to be able to compare results between different vehicles, wind speeds or vehicle scales. Non-dimensional quantities are also useful when setting up a numerical simulation to determine for example the cell sizes in the mesh.

#### 2.1.1 Force coefficients

The aerodynamic forces are made non-dimensional by density, area and velocity. By using coefficients it's easier to compare the aerodynamic performance of different vehicles. The drag coefficient is defined as

$$Cd = \frac{F_{drag}}{\frac{1}{2}\rho_{\infty}AV_{\infty}^2} \quad (2.1)$$

where  $A$  is a characteristic area and  $\rho$  is the fluid density. The  $\infty$  subscript denotes the free-stream values. For vehicles the characteristic area,  $A$ , is often chosen as the vehicle frontal area. The aerodynamic coefficients are often presented in terms of counts where one count is one thousandth of a coefficient as

$$0.001Cd = 1 \text{ count } Cd \quad (2.2)$$

#### 2.1.2 Front lift

The area of interest for this thesis is related to front lift. To define front lift we must first determine the point at which the sum of aerodynamic forces act. This point is called the centre of pressure (CoP) and is defined as the point where the sum of moments due to aerodynamic-forces is zero. The centre of pressure location in x-direction is defined as

$$CoP_x = \frac{\int x (\tau(x) + p(x)) dx}{\int \tau(x) + p(x) dx} \quad (2.3)$$

where  $\tau$  is the contribution due to wall shear stress and  $p$  is the contribution due to surface pressure. The front lift is found by taking the moment balance around the rear wheel contact patch and is defined as

$$Cl_{front} = \frac{Cm_{rear}}{l_{wb}}, \quad Cm_{rear} = CdZ + ClX \quad (2.4)$$

where  $l_{wb}$  is the wheel base (distance between front and rear contact patch) of the vehicle.  $Z$  and  $X$  is the vertical and horizontal distance respectively from the rear wheel contact patch to the centre of pressure. The total lift,  $Cl$ , equals the sum of front,  $Cl_{front}$  and rear lift,  $Cl_{rear}$ ; however the balance between front and rear is a function of  $Cd$ ,  $Cl$  and the location of centre of pressure, as seen in equation 2.4.

#### 2.1.3 Reynolds number

The Reynolds number is a non-dimensional quantity that defines the ratio between the inertial and viscous forces. It is used to scale fluid dynamics problems and gives an indication if a fluid flow is turbulent. The Reynolds number is defined as

$$Re = \frac{\rho_{\infty}V_{\infty}L}{\mu_{\infty}} \quad (2.5)$$

where  $L$  is a characteristic length and  $\mu_{\infty}$  is the free-stream viscosity . For vehicles  $L$  is chosen as the length of the vehicle. Fluid flows with high Reynolds numbers and regions of massive separation such as external vehicles aerodynamics are characterised by turbulence.

### 2.1.4 Pressure coefficient

Similarly to the force coefficients the pressure is also made non-dimensional. The pressure coefficient,  $C_p$ , describes the ratio of pressure forces to inertial forces and is defined as

$$C_p = \frac{p - p_\infty}{\frac{1}{2}\rho_\infty V_\infty^2} \quad (2.6)$$

Where  $p$  denotes pressure at the location  $C_p$  is measured and  $p_\infty$  is the free-stream pressure.

### 2.1.5 Cell size

When running fluid simulations special care has to be taken when designing the mesh. In order for wall functions to give good predictions the first cell centre height is important. The non-dimensional first cell centre height,  $y^+$  is defined as

$$y^+ = \frac{u_* \rho_\infty y}{\mu} \quad (2.7)$$

$$u_* = \sqrt{\frac{\tau_{wall}}{\rho_\infty}} \approx 0.05V_\infty$$

Similarly the mesh streamwise,  $s^+$  and spanwise,  $l^+$ , lengths can be defined the same way.

## 2.2 Governing equations

The FVM CFD simulations carried out in this thesis solve the discretized Navier-Stokes equation which describes how the fluid motion is governed. The fluid is considered a continuum at macroscopic length scales meaning that the molecular structure and molecular motion is ignored [7]. The fluid is considered Newtonian meaning that the shear stress is linearly dependant on the shear strain rate [8]. The Navier-Stokes equations can be derived by applying the conservation of mass and momentum to a fluid element. For incompressible flow and constant viscosity without body forces the Navier-Stokes equation, in Einstein notation, reads

$$\frac{\partial v_i}{\partial x_i} = 0 \quad (2.8)$$

$$\frac{\partial v_i}{\partial t} + \frac{\partial}{\partial x_j}(v_i v_j) = -\frac{1}{\rho} \frac{\partial P}{\partial x_i} + \nu \frac{\partial^2 v_i}{\partial x_j \partial x_j} \quad (2.9)$$

where  $\rho$  is the density,  $\mu$  is the viscosity of the fluid and the index  $i$  represents the direction ( $i = 1, 2, 3$ ). Equation 2.8 is the continuity equation and equation 2.9 is the momentum equation which together are called the Navier-Stokes equation. The partial differential equation that is the Navier-Stokes equation remains analytically unsolved except for simplified cases. In order to overcome this problem the Navier-Stokes equation is integrated over a control volume and discretized. The discretized Navier-Stokes equation can then be solved with numerical methods. Solving the discretized Navier-Stokes equation without further modification is called DNS (Direct Numerical Simulation). Performing a DNS requires that all temporal and spatial scales are resolved limiting the method to cases with low Reynolds number due to the large computational costs. DNS is however still useful with today's computing power as it is used as a tool to aid development of turbulence models [9].

## 2.3 Turbulence modelling

In order to reduce computational cost some form of averaging; for instance time- or volume-averaging is used. A consequence of averaging is that the number of unknowns exceed the number of equations, this is called the closure problem. To close and solve the averaged equations turbulence modelling is employed. Turbulent flow has no definition however it is characterised by high Reynolds numbers, diffusivity, dissipation, irregularity, it is three dimensional and occurs at scales much larger than molecular i.e. the continuum assumptions holds true [10]. Turbulent flow contains eddies or turbulent structures at different scales where the large eddies extract

their energy from the mean flow and the small eddies dissipate the energy as heat because of the viscosity (friction) in the fluid. The turbulence model used in this thesis is the SST (Shear Stress Transport)  $k-\omega$  IDDES (Improved Delayed Detached Eddy Simulation) model. The IDDES turbulence model is a combined RANS - LES model.

### 2.3.1 LES

LES (Large Eddy Simulation) is a method in which the Navier-Stokes equations are volume averaged (filtered) so that the large energy-containing eddies are resolved and the small dissipative eddies are modeled. The filter width is typically set as the cube root of the cell size [10] and the expected turbulent structures captured are larger than twice the cell size [11]. The flow is divided into a resolved and a modelled part as

$$\Phi = \bar{\Phi} + \Phi'' \quad (2.10)$$

where  $\bar{\Phi}$  denotes the resolved part and  $\Phi''$  is the modelled part. The filtered LES equation is derived by substituting equation 2.10 into the Navier-Stokes equation, equation 2.8 and 2.9; and then volume averaging. The filtered Navier-Stokes equation reads

$$\frac{\partial \bar{v}_i}{\partial x_i} = 0 \quad (2.11)$$

$$\frac{\partial \bar{v}_i}{\partial t} + \frac{\partial}{\partial x_j} (\bar{v}_i \bar{v}_j) = -\frac{1}{\rho} \frac{\partial \bar{P}}{\partial x_i} + \nu \frac{\partial^2 \bar{v}_i}{\partial x_j \partial x_j} - \frac{\partial \tau_{ij}}{\partial x_j} \quad (2.12)$$

where  $\tau_{ij}$  is the SGS (Sub-Grid-Scale) stress term. The SGS term reads

$$\tau_{ij} = \overline{v_i v_j} - \bar{v}_i \bar{v}_j \quad (2.13)$$

Note the addition of the SGS stress term compared to the unfiltered Navier-Stokes equation which is a direct consequence of the volume averaging. The SGS stress term is unknown since it depends on the resolved velocity field and thus needs to be modeled. There exists several models and the most simple rely on the Boussinesq assumption of eddy viscosity. Eddy viscosity models assume that the stresses due to turbulence is proportional to the mean rates of deformation according to

$$\tau_{ij} - \frac{1}{3} \delta_{ij} \tau_{kk} = -2\nu_{sgs} \bar{S}_{ij} \quad (2.14)$$

where  $\nu_{sgs}$  is the SGS viscosity and  $\bar{S}_{ij} = \partial \bar{v}_i / \partial x_j + \partial \bar{v}_j / \partial x_i$  is the resolved mean strain rate tensor. For the WALE model the  $\nu_{sgs}$  is computed as [10]

$$\begin{aligned} g_{ij} &= \frac{\partial \bar{v}_i}{\partial x_j}, g_{ij}^2 = g_{ik} g_{kj} \\ \bar{s}_{ij}^d &= \frac{1}{2} (g_{ij}^2 + g_{ji}^2) - \frac{1}{3} \delta_{ij} g_{kk}^2 \\ \nu_{sgs} &= (C_m \Delta)^2 \frac{(\bar{s}_{ij}^d \bar{s}_{ij}^d)^{3/2}}{(\bar{s}_{ij} \bar{s}_{ij})^{5/2} (\bar{s}_{ij}^d \bar{s}_{ij}^d)^{5/4}} \end{aligned} \quad (2.15)$$

The computational cost for LES is lower than that of DNS however the computational cost is still large for high Reynolds numbers due to the fine grid requirements near the wall [12] necessitating further modeling.

### 2.3.2 Unsteady-RANS

RANS (Reynolds Averaged Navier-Stokes) reduces the computational cost by computing a time averaged representation of the flow. The RANS equation is derived by decomposing the instantaneous quantities into a time-averaged mean and fluctuating part as

$$\Phi = \tilde{\Phi} + \Phi' \quad (2.16)$$

where  $\widetilde{\Phi}$  is the time-averaged mean quantity and  $\Phi'$  fluctuates around the mean. This is called the Reynolds decomposition. The time-averaged RANS equation is derived by substituting equation 2.16 into the Navier-Stokes equation, equation 2.8 and 2.9; and then time-averaging. The time-averaged Navier-Stokes equation reads

$$\frac{\partial \widetilde{v}_i}{\partial x_i} = 0 \quad (2.17)$$

$$\frac{\partial \widetilde{v}_i}{\partial t} + \frac{\partial}{\partial x_j} (\widetilde{v}_i \widetilde{v}_j) = -\frac{1}{\rho} \frac{\partial \widetilde{P}}{\partial x_i} + \nu \frac{\partial^2 \widetilde{v}_i}{\partial x_j \partial x_j} - \frac{\partial \widetilde{v}_i' v_j'}{\partial x_j} \quad (2.18)$$

The time dependent term on the left hand side is zero when time-averaging however for the Unsteady-RANS equation it is kept. As a consequence of averaging there is an additional unclosed term on the right hand side called the Reynolds stress tensor. The Reynolds stress tensor appears due to turbulence and is, in this thesis, modelled by the SST  $k - \omega$  turbulence model. Note the similarity between the filtered LES equation (2.12) and the time averaged URANS equation (2.18). The difference between the two methods is the amount of turbulence that is resolved or modelled, where LES resolves more of the turbulence.

### 2.3.3 SST $k - \omega$

The SST (Shear Stress Transport)  $k - \omega$  turbulence model is a two equation eddy viscosity turbulence model. The model solves the transport of turbulent kinetic energy,  $k$ , and depending on the distance to the nearest wall, the transport for specific dissipation rate,  $\omega$ , or the transport for turbulent dissipation,  $\varepsilon$ . The transport for  $k - \omega$  is solved for close to the wall and far from the wall it is solved with  $k - \varepsilon$ , in between the coefficients are blended between the two models. The SST  $k - \omega$  equation reads [10]

$$\frac{\partial k}{\partial t} + \frac{\partial}{\partial x_j} (\widetilde{v}_j k) = \frac{\partial}{\partial x_j} \left[ \left( \nu + \frac{\nu_t}{\sigma_k} \right) \frac{\partial k}{\partial x_j} \right] + P^k - \beta^* k \omega \quad (2.19)$$

$$\frac{\partial \omega}{\partial t} + \frac{\partial}{\partial x_j} (\widetilde{v}_j \omega) = \frac{\partial}{\partial x_j} \left[ \left( \nu + \frac{\nu_t}{\sigma_\omega} \right) \frac{\partial \omega}{\partial x_j} \right] + \alpha \frac{P^k}{\nu_t} - \beta \omega^2 + 2(1 - F_1) \sigma_\omega 2 \frac{1}{\omega} \frac{\partial k}{\partial x_i} \frac{\partial \omega}{\partial x_i}$$

$$F_1 = \tanh(\xi^4), \quad \xi = \min \left[ \max \left\{ \frac{\sqrt{k}}{\beta^* \omega d}, \frac{500\nu}{d^2 \omega} \right\}, \frac{4\sigma_{\omega_{k-\varepsilon}} k}{CD_\omega d^2} \right]$$

$$CD_\omega = \max \left\{ 2\sigma_{\omega_{k-\varepsilon}} \frac{1}{\omega} \frac{\partial k}{\partial x_i} \frac{\partial \omega}{\partial x_i}, 2\sigma_{\omega_{k-\varepsilon}} 10^{-20} \right\}$$

$$\nu_t = \frac{a_1 k}{\max(a_1 \omega, |\bar{s}| F_2)}, \quad F_2 = \tanh \left( \left[ \max \left\{ \frac{k^{1/2}}{\beta^* \omega d}, \frac{500\nu}{d^2 \omega} \right\} \right]^2 \right)$$

where  $d$  denotes the distance to the closest wall and the constants are given by

$$\begin{aligned} \beta^* &= 0.09 & a_1 &= 0.3 \\ \alpha_{k-\omega} &= \frac{\beta_1}{\beta^*} - \sigma_{w,k-\omega} \frac{\kappa^2}{\sqrt{\beta^*}}, & \kappa &= 0.41, & \beta_{k-\omega} &= 3/40, & \sigma_{k,k-\omega} &= 0.85, & \sigma_{w,k-\omega} &= 0.5 \\ \alpha_{k-\varepsilon} &= \frac{\beta_2}{\beta^*} - \sigma_{w,k-\varepsilon} \frac{\kappa^2}{\sqrt{\beta^*}}, & \kappa &= 0.41, & \beta_{k-\varepsilon} &= 0.0828, & \sigma_{k,k-\varepsilon} &= 1, & \sigma_{w,k-\varepsilon} &= 0.856. \end{aligned} \quad (2.20)$$

The SST  $k - \omega$  turbulence model utilises the strengths of the standard  $k - \omega$  close to the wall and the strengths of  $k - \varepsilon$  far from the wall. The blending of coefficients is applied as

$$\Phi = F_1 \Phi_{k-\omega} + (1 - F_1) \Phi_{k-\varepsilon} \quad (2.21)$$

where  $\Phi$  denotes the coefficient.

### 2.3.4 DES

DES (Detached Eddy Simulation) combines the LES and Unsteady-RANS approach so that the flow is solved by Unstead-RANS and LES in different regions. The benefit of using a combined approach is that the boundary layer can be solved using Unsteady-RANS while the large separated flow regions such as the vehicle wake is calculated with LES. The near wall grid requirements for LES with good resolution is  $s^+ < 100$  and  $l^+ < 30$ ; for RANS the grid requirements for good resolution are  $s^+ < 1000$  and  $l^+ < 200$ . The grid resolution requirements near the wall can then be relaxed for the combined LES-URANS making the method more affordable. The grid requirements are however not relaxed in the far field, for large separated regions like the wake of a vehicle the same grid requirements are justified for LES and DES [13]. The dissipation term for the DES formulation of SST  $k - \omega$  is modified based on the work by Meneter and Kuntz [14] and reads

$$\varepsilon = \beta^* k \omega \rightarrow \beta^* k \omega F_{DES}, \quad F_{DES} = \max \left\{ \frac{L_t}{C_{DES} \Delta}, 1 \right\} \quad (2.22)$$

$$\Delta = \max(\Delta_i), \quad L_t = \frac{\sqrt{k}}{\beta^* \omega} \quad (2.23)$$

where  $\Delta_i$  is the maximum local grid spacing in direction 1, 2 or 3.  $C_{DES}$  is given by

$$\begin{aligned} C_{DES} &= C_{DES,k-\omega} F_1 + C_{DES,k-\varepsilon} (1 - F_1) \\ C_{DES,k-\omega} &= 0.78, \quad C_{DES,k-\varepsilon} = 0.61 \end{aligned} \quad (2.24)$$

base on the work by Travin, A., Shur, M. L., Strelets, M. Kh., and Spalart, P. R. [15] The DES formulation requires a carefully constructed grid since the switch is dependent on the local grid spacing  $\Delta$  in equation 2.22. If the mesh becomes too fine in the boundary layer there is a risk of switching to LES too early leading to poorly resolved LES in the boundary layer.

### 2.3.5 DDES

In order to reduce grid induced flow separation, caused by the model to switching to LES too early, Meneter and Kuntz [14] proposed a method to protect the boundary layer. The method is called DDES (Detached Delayed Eddy Simulation). Equation 2.22 is modified as

$$F_{DES} = \max \left\{ \frac{L_t}{C_{DES} \Delta} (1 - F_2), 1 \right\}. \quad (2.25)$$

The DDES formulation does not remove the problem of switching to LES in the boundary layer completely but the problem is reduced by an order of magnitude [14].

### 2.3.6 IDDES

The turbulence model used in this thesis work is the IDDES (Improved Delayed Detached Eddy Simulation) SST  $k - \omega$  formulation. The IDDES formulation combines DDES with WMLES (Wall Modelled Large Eddy Simulation) allowing WMLES to be used when the grid resolution is sufficiently fine. The WMLES approach solves more of the flow close to the wall with LES where only the inner part of the boundary layer is solved with URANS, compared to DDES where the aim is to treat the entire boundary layer with URANS. The dissipation term in the DES formulation is modified as

$$\varepsilon = \beta^* k \omega F_{DES} \rightarrow \frac{k^{3/2}}{l_{HYBRID}} \quad (2.26)$$

where the IDDES length scale,  $l_{HYBRID}$ , is given by

$$l_{HYBRID} = \tilde{f}_d (1 + f_e) L_t + (1 - \tilde{f}_d) C_{DES} \Delta_{IDDES} \quad (2.27)$$

The emepric blending function,  $\tilde{f}_d$ , and the elevating function,  $f_e$ , are given by

$$\begin{aligned}\tilde{f}_d &= \max \left( \tanh \left[ (C_{dt} r_{dt})^{C_{dt2}} \right], \min \left[ 2e^{-9\alpha^2}, 1 \right] \right) \\ \alpha &= 0.25 - \frac{d}{\Delta} \\ r_{dt} &= \frac{\nu_t}{\kappa^2 d_\omega^2 \sqrt{1/2(S_{ij}^2 + \Omega_{ij}^2)}} \\ f_e &= \max \left[ (f_{e1} - 1), 0 \right] \Psi f_{e2} \\ f_{e1} &= \begin{cases} 2e^{-11.09\alpha^2}, & \alpha \geq 0 \\ 2e^{-9.0\alpha^2}, & \alpha < 0 \end{cases} \\ f_{e2} &= 1 - \max \left( \tanh \left( (C_t^2 r_{dt})^3 \right), \tanh \left( (C_t^2 r_{dt})^{10} \right) \right) \\ r_{dt} &= \frac{\nu}{\kappa^2 d_\omega^2 \sqrt{1/2(S_{ij}^2 + \Omega_{ij}^2)}}\end{aligned}$$

where  $\Psi$  is a low-Reynolds number correction function [16],  $S_{ij}$  is the the strain rate tensor and  $\Omega_{ij}$  is the vorticity tensor. The coefficients are given by

$$C_w = 0.15 \quad C_{dt1} = 20, \quad C_{dt2} = 5, \quad C_t = 1.87. \quad (2.28)$$

The mesh length scale,  $\Delta_{IDDES}$ , is modified for IDDES as

$$\Delta_{IDDES} = \min(\max\{0.15d, 0.15\Delta, \Delta_{min}\}, \Delta) \quad (2.29)$$

The application of IDDES brings no additional cost over (D)DES [17].

## 2.4 Wall treatment

High  $y^+$  wall treatment is used to obtain the reference velocity, turbulent production and specific dissipation at the wall. When using wall functions the first cell centre height,  $y_+$ , should reside in the log law region of the boundary layer ( $30 \leq y^+ \leq 200$ ). The alternative to using a high  $y^+$  wall treatment is to use a low  $y^+$  wall treatment where the viscous sub-layer is resolved, this does however require 10-20 cells in the boundary [18] making the method prohibitively expensive for flows with high Reynolds numbers.

## 2.5 Porous media

The condenser, charge air cooler and radiator exchange heat with the oncoming air through fins, these fins are in turn in contact with pipes that have coolant pumped through them. Solving the flow through each fin is prohibitively expensive necessitating the use of a porosity model. The porosity is modelled as an inertial and viscous coefficient according to

$$\frac{\Delta p}{L} = -(P_i |v| + P_v) v \quad (2.30)$$

where  $P^i$  is the inertial coefficient and  $P^v$  is the viscous coefficient. The coefficients are found through experiments where the velocity and pressure drop across the radiator is measured. The modelled porosity is implemented as an additional source term in the Navier-Stokes equation for the radiator regions. The porosity coefficients found through experiments only describe the resistance in the direction aligned with the flow, the vertical and horizontal coefficients are usually taken as two or three orders of magnitude larger.

### 3 Method

The method for running the CFD simulations in this thesis work is comprised of geometry preparation, mesh generation and simulation on a computational cluster. When the simulations are finished the results are post-processed in order to extract useful information such as aerodynamic forces,  $Cd$ ,  $Cl$  or surface pressures,  $Cp$ . The simulation setup and settings used will be presented in this chapter as well as the post processing methods used.

#### 3.1 Configurations

Three configurations were used to investigate the effect of cooling flow for different underbody configurations on front lift as well as investigate the trend capturing capability of the FVM solver between configurations. The configurations used are; exhaust cover on, exhaust cover off and engine cover off. The configurations are named A, B and C respectively and can be seen in Figure 3.1 below. Each configuration is run at three operating conditions; open cooling, closed cooling and AGS closed

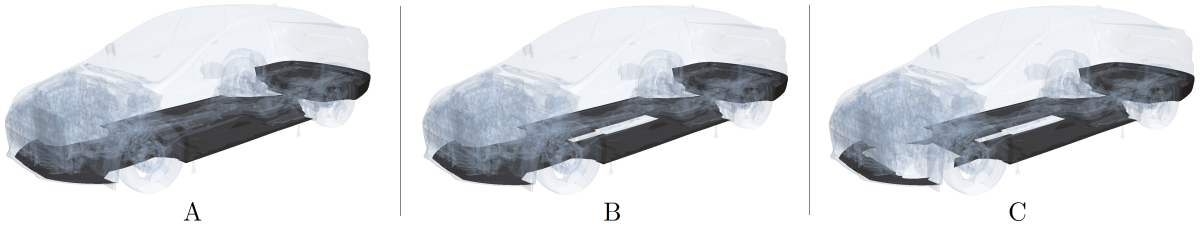


Figure 3.1: *Vehicle configurations*

as shown below in Figure 3.2. The blanked cooling condition is run with a fully detailed engine compartment, the only difference between the open and closed condition is the additional surface blanking the grille. The AGS is kept open for both the open and closed cooling condition.

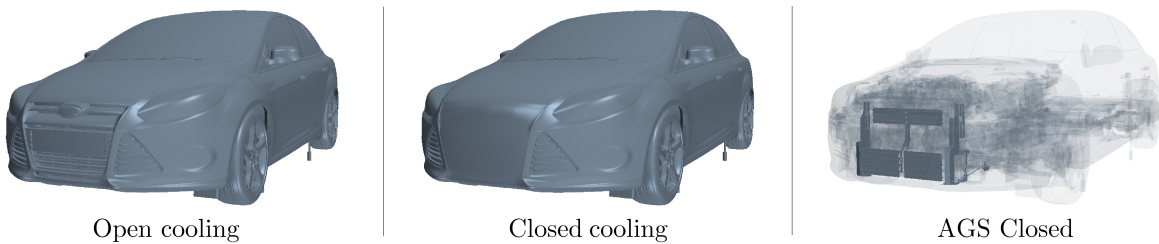


Figure 3.2: *Vehicle operating conditions*

##### 3.1.1 Cooling flow

The cooling flow is defined as the difference between the open and closed operating condition. The cooling flow and the effect it has can be taken on any quantity such as,  $Cl$ ,  $Cd$  or surface pressure. For the drag coefficient it is defined as

$$\Delta Cd = Cd_{open} - Cd_{closed} \tag{3.1}$$

where  $\Delta Cd$  is the cooling drag coefficient and  $Cd_{open}$ ,  $Cd_{closed}$  is the drag coefficient for the open and closed configuration respectively. It should be noted that the fully closed operating condition is only used for aerodynamic analysis to determine the aerodynamic effect cooling flow has on the vehicle, however the AGS closed operating condition is used in real world driving situations when less cooling flow is needed to reduce drag actively.

### 3.1.2 $\Delta$ Cooling flow between configurations

The delta cooling flow between two configurations is used to describe how the cooling flow is effected by removing for example the exhaust shield. The delta cooling flow drag is defined as

$$\begin{array}{r}
 Cd_{A, Open} \\
 Cd_{A, Closed}
 \end{array}
 \left. \vphantom{\begin{array}{r} Cd_{A, Open} \\ Cd_{A, Closed} \end{array}} \right\} \Delta Cd_A
 \left. \vphantom{\begin{array}{r} \Delta Cd_A \\ \Delta Cd_B \end{array}} \right\} \Delta\Delta Cd_{B-A}
 \\
 \begin{array}{r}
 Cd_{B, Open} \\
 Cd_{B, Closed}
 \end{array}
 \left. \vphantom{\begin{array}{r} Cd_{B, Open} \\ Cd_{B, Closed} \end{array}} \right\} \Delta Cd_B
 \tag{3.2}$$

where  $\Delta\Delta Cd_{B-A}$  is the difference in cooling drag between configuration B and A.  $\Delta\Delta Cd_{B-A}$  would in this case describe how the cooling drag is reduced or increased by removing the exhaust shield.

## 3.2 Wind tunnel

The wind tunnel results that are used for comparison is from Pinifarina wind tunnel in Turin, Italy. The wind tunnel is capable of a maximum velocity of 70 m/s, measuring lift and drag with an accuracy of  $\pm 0.3N$ ; with a velocity uniformity ( $\Delta V/V$ ) of  $\leq \pm 0.5\%$  [19]. The wind tunnel uses a T-belt ground simulation system with one narrow central belt and two front side belts which is also used in the virtual wind tunnel as shown below in Figure 3.3. The ground simulation system also includes tangential blowers and rollers for wheel rotation.



Figure 3.3: *CFD and Pinifarina wind tunnel*

## 3.3 Simulation

The FVM simulations were meshed, run and post processed using STAR-CCM+ from CD-Adapco. STAR-CCM+ is a software that according to CD-Adapco is "The world's most comprehensive engineering simulation inside a single integrated package" [20]. The LBM simulations were run prior to the thesis start at Ford and, as stated in the limitations, the methodology and theory for the LBM simulations will not be covered in the thesis.

### 3.3.1 Geometry

The geometry was prepared in Ansa by BETA CAE Systems which is a software that can be used for CAD clean up and mesh generation. The meshing procedure in STAR-CCM+ uses features (explained in the next section) that relaxes the need of thorough CAD clean up. STAR-CCM+ can however not handle zero thickness surfaces in the meshing procedure, which needs to be fixed in Ansa. All zero thickness surfaces were duplicated, offset and then joined together to created walls with volume.

## Real & Virtual geometry

The vehicle used in the wind tunnel has taped gaps and a 3D scanned floor in order to reduce the geometrical differences between the virtual and real vehicle. By taping and preventing flow in small gaps the mesh requirements are reduced since a gap needs several cells in order to be captured correctly in simulations. Examples of the taped geometry can be seen below in Figure 3.4 where the cooling blanking is done by taping



Figure 3.4: *Taped geometry*

the grille. There does however exist geometrical differences between the virtual and physical vehicle, for example in the cooling blanking where in CFD it's represented by a smooth surface which can be seen above in Figure 3.3. The wind tunnel geometry is not represented in the simulation, however, as mentioned previously, the T-belt ground simulation system used in the Pinifarina wind tunnel is replicated.

### 3.3.2 Mesh

The meshing procedure used in STAR-CCM+ consists of surface wrapping, surface re-meshing, surface repair and volume meshing. The meshing procedure is automated in STAR-CCM+ so that each step is carried out sequentially once meshing is started. The mesh generated is hexahedral consisting of  $\sim 74$  million cells (depending on configuration) with four prism layers on external surfaces.

#### Surface meshing

Volume meshing in STAR-CCM+ has three requirements on the surface mesh; It has to be manifold, non-intersecting and closed. Poor quality in the volume mesh can, according to STAR-CCM+ best practice guidelines [21], often be tracked down to problems in the surface mesh. The surface mesh is generated in STAR-CCM+ using the surface wrapper, surface remesher and automatic surface repair. The surface wrapper, wraps the geometry in a triangulated mesh which removes potential CAD problems such as open holes, disconnected and overlapping surfaces. After wrapping the surface it is remeshed with the surface remesher. The surface remesher creates a triangulated surface mesh suitable for volume meshing. The surface remesher can however cause issues in the surface mesh for complex geometries when used together with the surface wrapper.

## Volume meshing

The automatic surface repair tool is run before volume meshing to remove potential issues created in the surface remeshing such as intersecting surfaces. The volume mesh is then created by the trimmed cell mesher which cuts a hexahedral template mesh around the surface mesh. Finally prism cells are added to create a high quality volume mesh at the surface suitable for the wall functions used in the solver. Figure 3.5 illustrates the

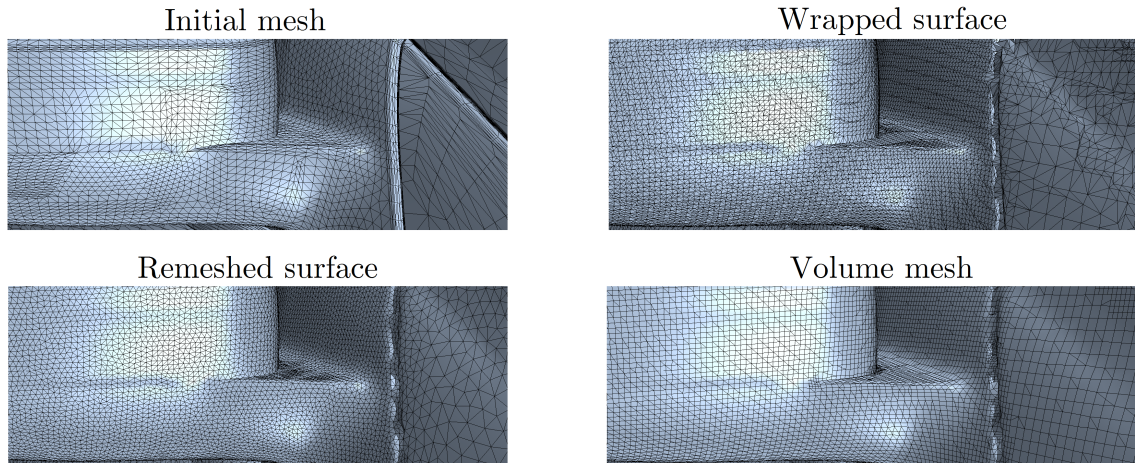


Figure 3.5: Surface mesh generated from the different meshing operations in STAR-CCM+

mesh at the surface of the wing mirrors, generated from the different meshing operations as well as the initial mesh. The surface mesh is refined at the grille and in areas of high gradients such as the A-pillars. The volume refinements used is shown below in Figure 3.6 and were placed in areas of high gradients based on results from a previously solved flow field for the vehicle. The cell count was kept below 80 million cells in order to give

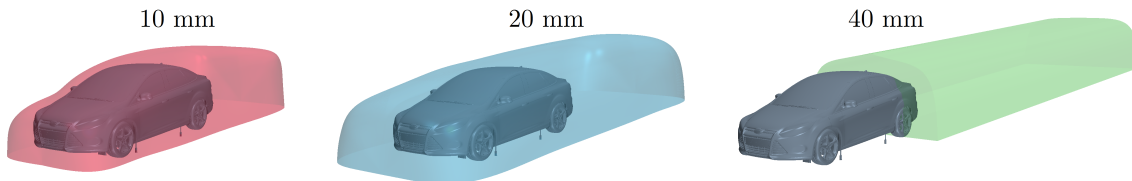


Figure 3.6: Pinifarina wind tunnel with Ford Focus

a fair comparison between the LBM and FVM simulations as well as keep the computational cost and time reasonable. The volume mesh generated is shown in Figure 3.7 on a plane located at the centreline of the vehicle.

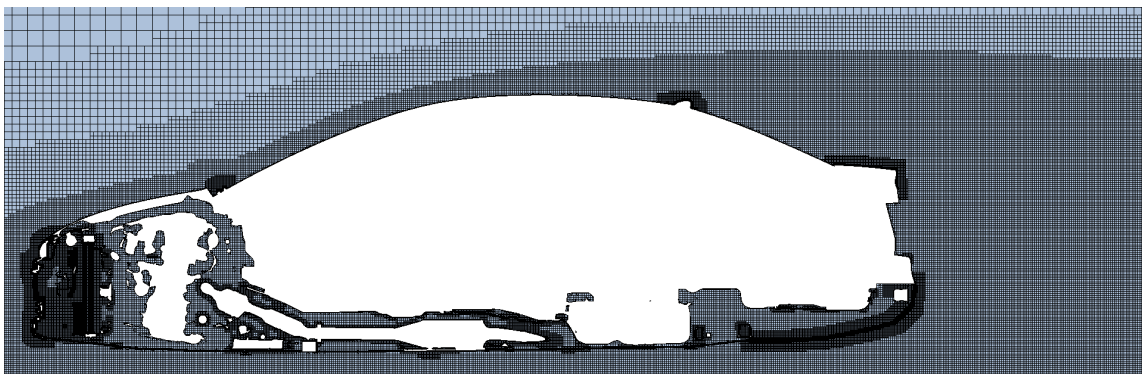


Figure 3.7: Volume mesh at the centerline

### 3.3.3 Simulation setup

The simulation setup used is based on a standard procedure used at Ford for FVM simulation. The simulation is run unsteady for a physical time of three seconds. Three seconds equates to  $\sim 2$  flow passages through the wind tunnel or  $\sim 26$  flow passages along the vehicle length. The unsteady flow field is averaged for the last one and a half seconds to compute the averaged flow field and aerodynamic forces. The FVM simulations were run for  $\sim 23$  thousand CPU hours and the equivalent LBM simulation  $\sim 19$  thousand hours on the same computational cluster, making the cost comparable between the two solvers. The FVM simulation settings are listed in Table 3.1 below.

<b>Turbulence model</b>	IDDES SST $k - \omega$
<b>Temporal discretization</b>	2nd-order
<b>Time-step</b>	$2.5 \times 10^{-4}$ s
<b>Physical total time</b>	3 s
<b>Velocity</b>	140 km/h
<b>Cell count</b>	$\sim 74 \times 10^6$
<b>Tyre rotation</b>	Moving wall
<b>Rim rotation</b>	MRF
<b>Inner iterations</b>	4
<b>Solver</b>	Segregated
<b>Wall treatment</b>	All $y^+$
<b>Gradients</b>	Hybrid Guass-LSQ
<b>Radiator model</b>	Porous region

Table 3.1: CFD Settings

More information about the specific settings used can be found in the user guide [16]. As stated in the theory the turbulence model used is the IDDES SST  $k - \omega$  turbulence model which is a combined RANS-LES model. The IDDES Blending function shows where the flow is solved with Unsteady-RANS (IDDES Blending function = 1) and where is it solved using LES (IDDES Blending function = 0). As Figure 3.8 illustrates it can be seen

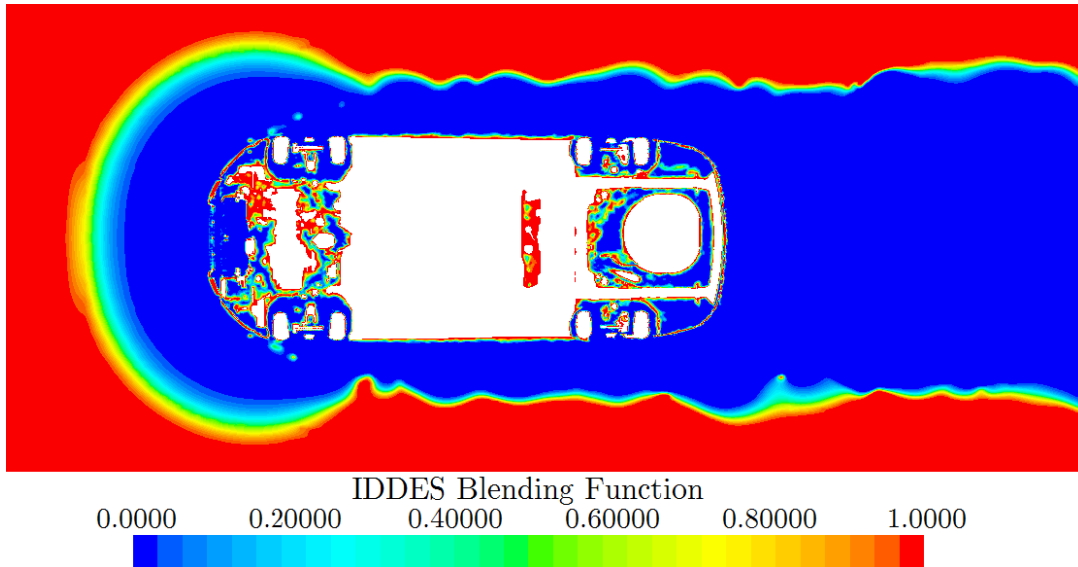


Figure 3.8: *IDDES Blending factor - Top view*

that the near wall flow field is solved with Unsteady-RANS while the large separated areas such as the wake is solved using LES.

### Rim rotation

The rim rotation is simulated with a MRF (Moving Reference Frame) approach. The MRF approach solves the Navier-Stokes equations in a rotating frame of reference where the spokes are seen as stationary and the fluid is moving. This is also called the frozen rotor approach since the rim is stationary and the fluid is given the equivalent rotation instead. The alternative to MRF is Sliding mesh which rotates the rim (slides the mesh) each time-step. The MRF approach has been shown to be less accurate than sliding mesh [22], however it was found that the simulation cost for sliding mesh was prohibitively high which is why MRF was used instead.

### Wind tunnel

The wind tunnel used in the simulations is shown below in Figure 3.9 where the length  $L$  is defined as one car length. The T-belt ground simulation system used in the Pinifarina wind tunnel is modelled in the virtual wind

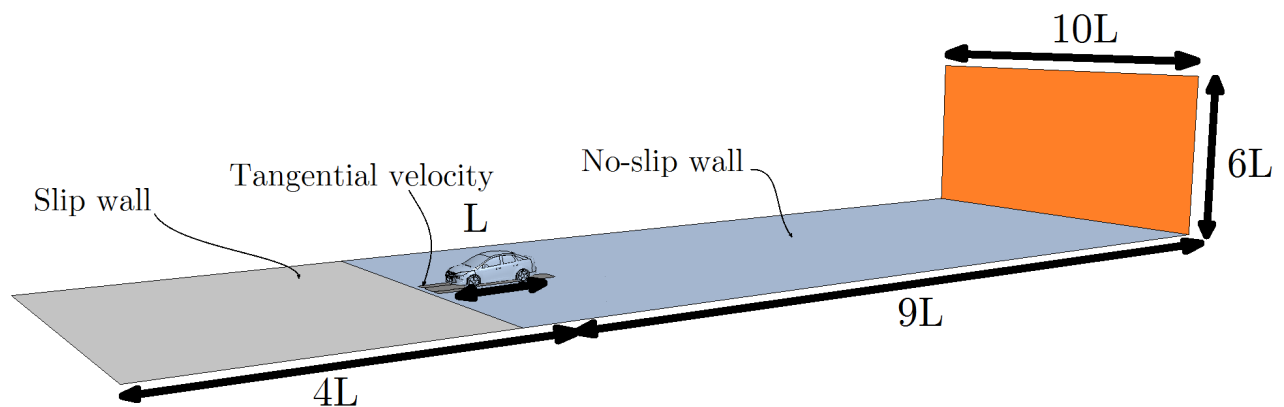


Figure 3.9: *Simulation wind tunnel*

tunnel as well. Upstream of the vehicle the ground is simulated with a slip condition, the belt is simulated as a moving wall and the rest as a stationary wall. It should however be noted that the virtual and real wind tunnel have different dimensions.

### 3.4 Post-processing

The post-processing of the simulation and wind tunnel results was done in the softwares Matlab and STAR-CCM+. Matlab, which is a software that can be used for numerical computations and data visualisation, was used to create plots comparing the results between the numerical solvers and the wind tunnel results. Matlab was also used to create Accumulated 1D and Integrated 2D plots from the CFD simulation results, which will be described in this section. Plotting the distribution of aerodynamic quantities gives an unique insight in how the aerodynamic forces are distributed (as predicted by CFD), this is something that is not possible to do in the same extent for real world wind tunnel tests.

#### 3.4.1 Accumulated 1D

The simulation results were post-processed in Matlab to create Accumulated 1D plots. The time averaged surface pressures and stresses were exported from STAR-CCM+ together with the cell centre position and cell surface area. The exported values are then imported into Matlab and used to calculate quantities such as drag and front lift. The imported surface values are sorted based on position along the vehicle to create "slices" of integrated quantities. As shown in Figure 3.10a the car is split into slices where the quantities such as drag is

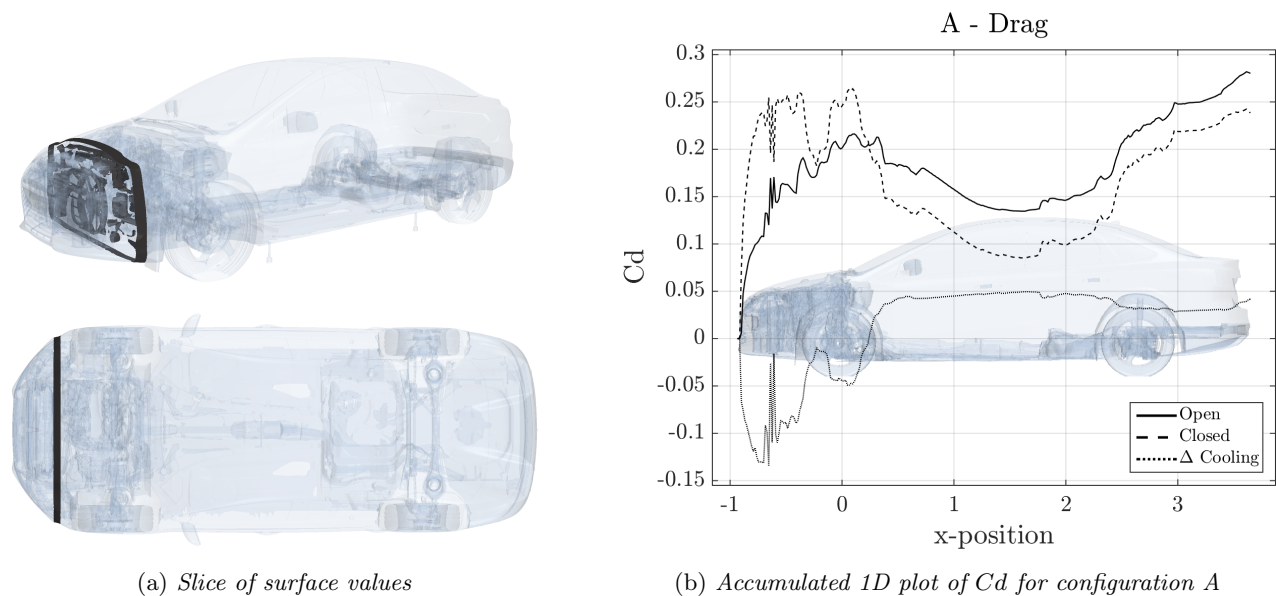


Figure 3.10: Accumulated 1D plot

integrated for each slice. The drag of each slice is then summed along the vehicle to create a one-dimensional line showing how the drag accumulates along the car, as shown in Figure 3.10b. The drag coefficient seen at the end of the car is then the total drag of the car. The plot includes the values for the open and closed operating condition as well as the cooling drag i.e. the difference between the open and closed lines.

### 3.4.2 Integrated 2D

The 1D Accumulated values describes how the aerodynamic forces are accumulated along the vehicle, however it gives little insight in what areas of the vehicle are causing the dips and peaks seen in the 1D plot. Using the same method as for the accumulated values the vehicle is sliced once more along the width to create squares which can be seen in Figure 3.11a. The values of each square is integrated and then plotted on a two-dimensional grid as shown in Figure 3.11b. This process is done twice; one time for each view, side and top. It is worth noting that the values for the Integrated 2D plot is not accumulated along the car as it is for the Accumulated 1D plot. The benefit of using a two-dimensional representation compared to commonly

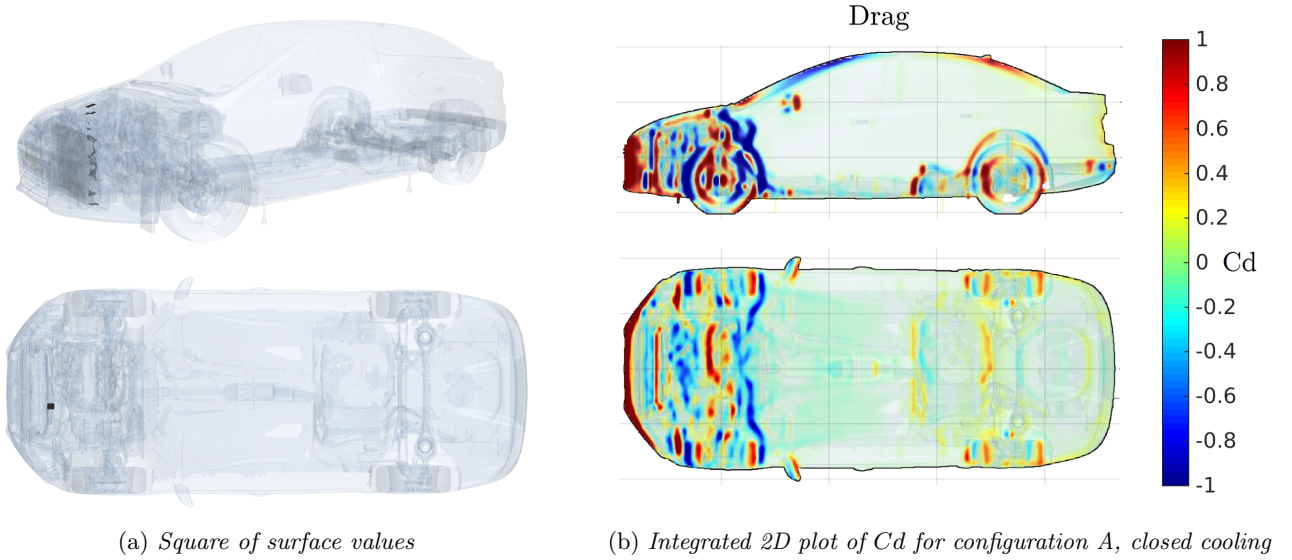


Figure 3.11: *Integrated 2D plot*

used three-dimensional plots is that the forces on all the surfaces, internal and external, can be presented in one figure. The Integrated 2D plots are also used to plot the force distribution change, ( $\Delta$ ), by plotting the difference between the open and closed operating condition. It should be noted that the Integrated 2D plots only give hints of areas of interest and need to be supported by additional post-processing such as plots of surface pressure.

### 3.4.3 Mass flow

The mass flow through the rims and at control planes seen in Figure 3.12 is used to compare the mass flow change between open and closed cooling. The mass flow coefficient,  $C\dot{m}$ , is normalised by the freestream mass flow through the same plane as

$$C\dot{m} = \frac{\dot{m}}{\rho V_{\infty} A} \quad (3.3)$$

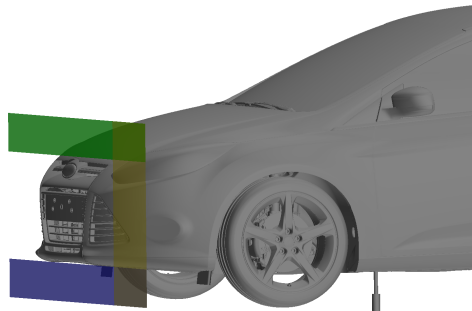


Figure 3.12: *Control planes used to measure mass flow around the vehicle*

## 4 Results

The results presented in this chapter are divided into two sections, the first section covers the results from the FVM simulations that are compared to the wind tunnel and LBM solver, such a drag and pressure probe measurements. The second section focuses on the front lift and cooling drag interaction where the results from the FVM simulations are used to investigate the interaction. The results are limited to reduce repetition of similar results between all nine simulations. Results for configuration A will be presented and complemented with results from configuration B and C. As mentioned previously, the vehicle and configurations used for the analysis in this thesis is not a production vehicle and is only used for aerodynamic investigations.

### 4.1 Wind tunnel and numerical comparison

This section contains results for the open, closed and AGS closed operating condition. The results for wind tunnel tests, FVM simulations and LBM simulations are presented to compare the accuracy and trend predicting capability of the two numerical solvers. Absolute numbers from the wind tunnel experiments are hidden for confidentiality, however deltas between experiments such as cooling drag is presented.

#### 4.1.1 Total values

The force coefficients for drag are presented below in Figure 4.1. The results are presented for the open and closed operating condition where the bar lengths represent the difference between open and closed cooling and is displayed in terms of counts as an underlined number to the left of the bars. For case A the cooling drag,  $\Delta Cd$ , is 34 counts. The dotted lines between the bars show the direction of the trend between configurations. The

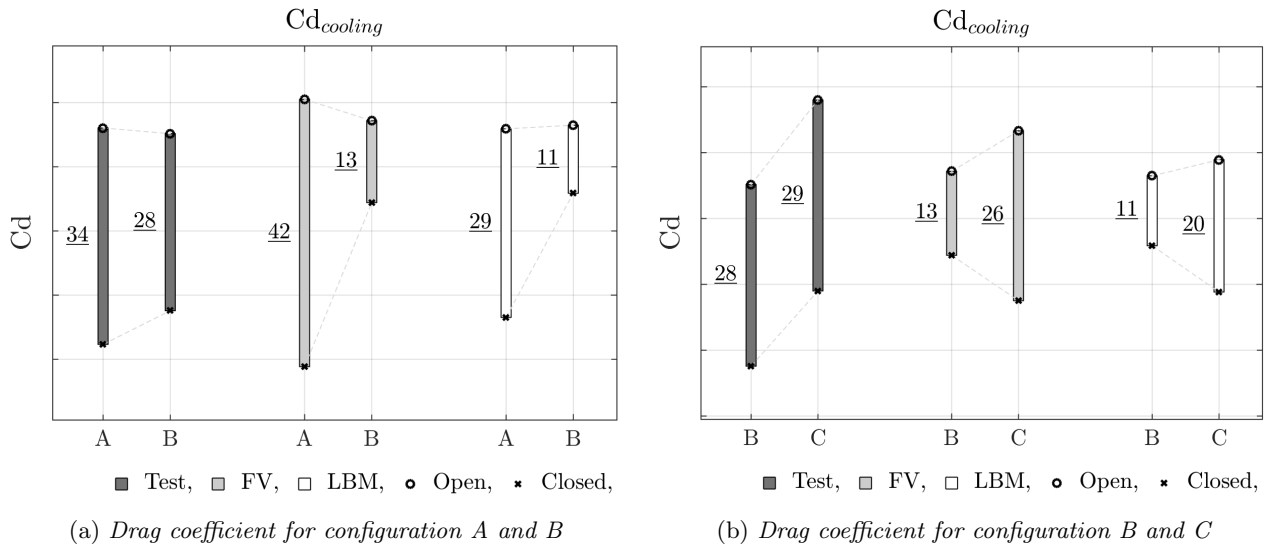


Figure 4.1:  $Cd$  for configuration A, B and C

change when going from configuration A to configuration B (removing the exhaust shield) is shown in Figure 4.1a. The change when going from configuration B to configuration C (removing the engine shield) is shown in Figure 4.1b. For open cooling the drag is predicted within five counts between the two numerical solvers and is close to wind tunnel results. For closed cooling the results from the numerical solvers are close to the wind tunnel results for configuration A and C where as the cooling drag for configuration B is underpredicted by both numerical solvers. Looking at the trends when going from configuration A to B or B to C there is little difference between the two numerical solvers with both solvers predicting the opposite trend for closed cooling going from configuration B to C.

The total front lift predictions, shown below in Figure 4.2, are, similarly to the drag predictions, close between

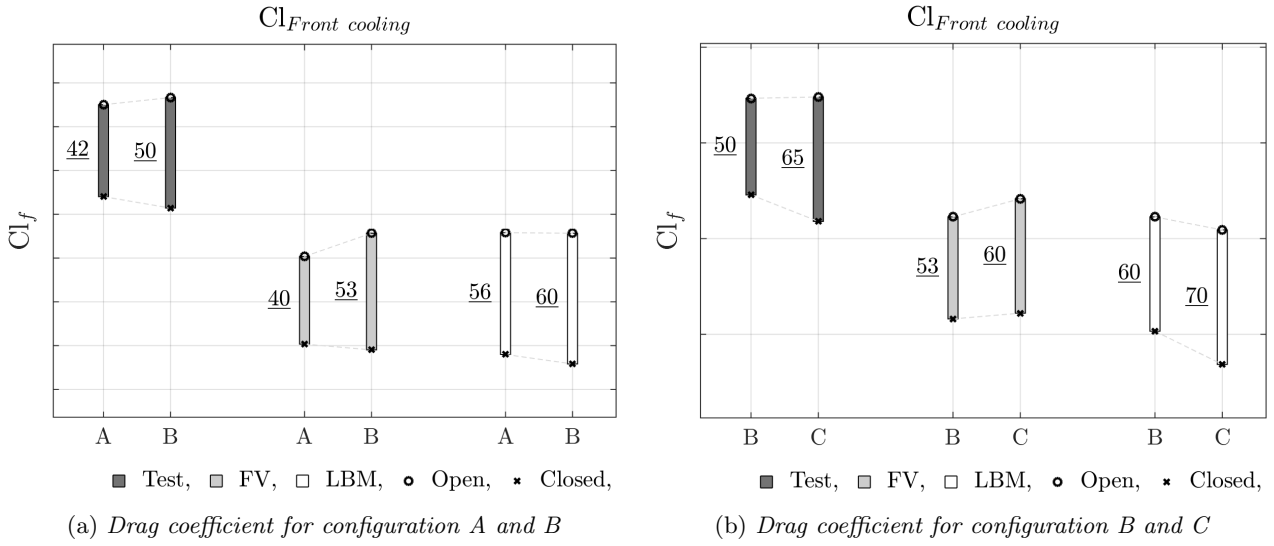


Figure 4.2:  $Cl_f$  for configuration A, B and C

the two numerical solvers; however the values are offset from the wind tunnel results by  $\sim 60-70$  counts. Based on the predicted absolute values and trends when comparing the the solvers to the wind tunnel results it is not clear which solver has better absolute or trend predicting capability.

### 4.1.2 Pressure probes

The wind tunnel testing includes measurements from pressure probes located on the hood, in the engine bay and below the front bumper. The pressure probe locations for the centerline probes and engine bay probes can be seen in Figure 4.3.

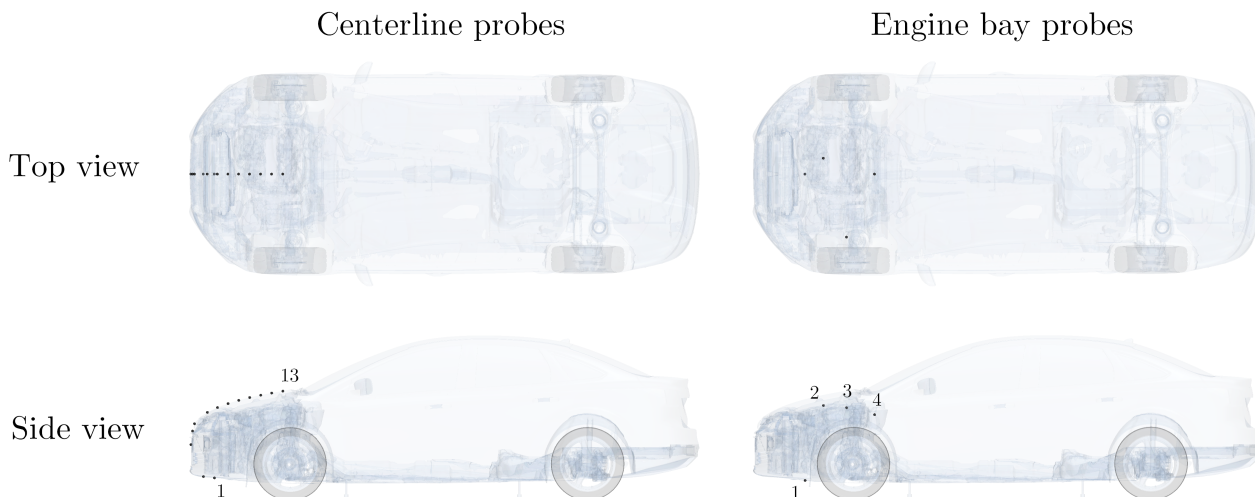


Figure 4.3: *Pressure probe locations - Centerline and Engine bay*

The hood pressure probes and front bumper pressure probes are placed as an array seen in Figure 4.4. The pressure probe values are plotted as a 2D surface. In order to put the pressure probe results in perspective

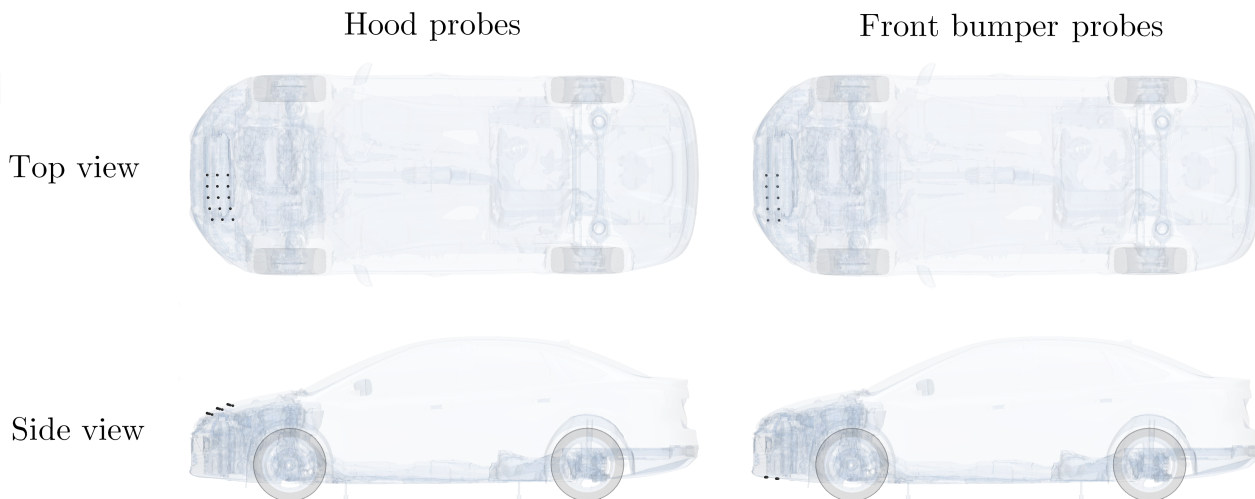


Figure 4.4: *Pressure probe locations - Hood and Front bumper*

examples of how pressure corresponds to changes in drag, lift and front lift are given below in Table 4.1. Each example presents how much the force changes (in counts) when the pressure on top of the hood or on the fire wall is increased by 0.1  $C_p$ . The values presented in the table consider a uniform pressure increase and only show the force change on the given part.

	$Cl$	$Cd$	$Cl_f$
<b>Fire wall</b>	9	30	14
<b>Hood</b>	-48	14	-50

Table 4.1: Force change (in counts) from 0.1  $C_p$  increase

## Centerline probes

The centerline probe results from the FVM, LBM and wind tunnel are shown in Figure 4.5 for configuration A. Positive pressures are displayed with markers outside the vehicle and negative inside. The distance between the probe values and the line joining the probes is proportional to the pressure at each point. A scale is provided close to the wind screen for reference. For Figure 4.5 the scale goes from  $C_p = -1$  to  $C_p = 1$ , it should be noted that the scale changes to highlight the differences. The open and closed cooling is plotted side by side in Figure 4.5 where the left plot shows the values for open cooling and the right the values for closed.

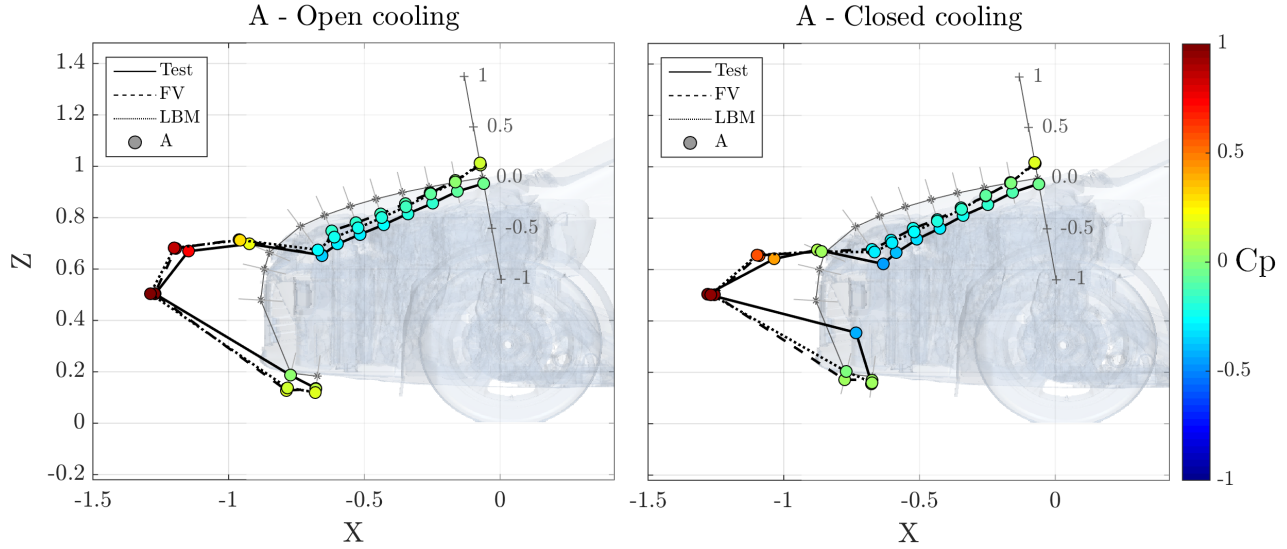


Figure 4.5: Centerline probe - Configuration A, Open and Closed cooling

The numerical solvers predict similar results and are offset from the wind tunnel results. The centerline pressure probe results for closed cooling significantly differ from the numerical results for the probe located at the lower front bumper, probe number two. This result is thought to be due to a geometrical difference between the real and virtual car causing the probe in the wind tunnel results to be in a region of separated flow which in turn is causing the low pressure seen in the wind tunnel results. The difference in pressure between the open and closed pressure probes is used to plot the effect cooling flow has on pressure,  $\Delta C_p$ , as shown in Figure 4.6. Note the scale is decreased by half for the cooling flow pressure plot. As seen in the results in Figure 4.6

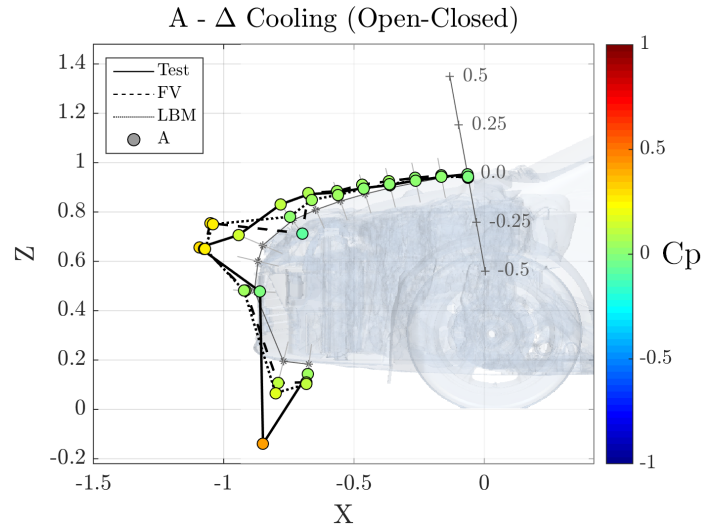


Figure 4.6: Centerline probe -  $\Delta C_{pA}$

the numerical solvers are predicting similar pressures except for the probe located at the start of the hood (probe number eight). This probe is located in a area of high pressure gradient meaning a small difference in the predicted pressure distribution between the solvers can have a large impact on the pressure measured at that location. We can also see that the pressures on the hood are close between the numerical solvers and the wind tunnel results. Probe number two is, as discussed previously, thought to be differing due to a geometrical difference between the real and simulated vehicle. On the front of the hood there are difference between the wind tunnel results and the numerical results. This difference might be due to geometrical differences in the blanking between the real and simulated car which will be discussed more in the Discussion chapter, page 33. As describe in the method the delta cooling between configurations is also investigated to see how the

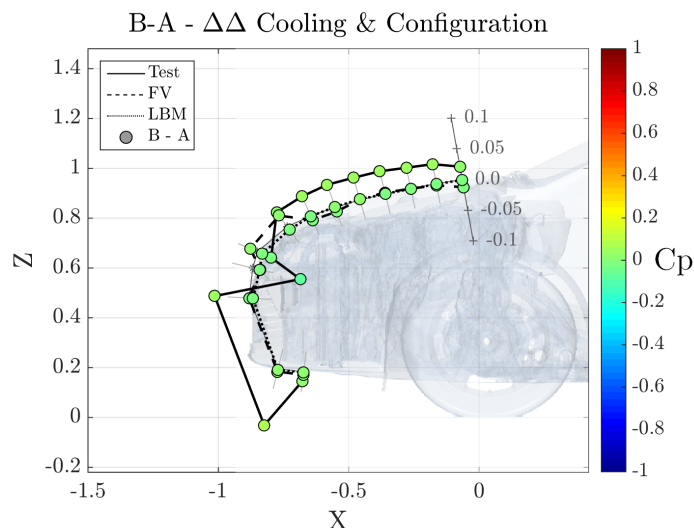


Figure 4.7: Centerline probe -  $\Delta\Delta C_{p_{B-A}}$

numerical solvers capture cooling flow trends between configurations. The cooling pressure difference between configuration B and A are plotted in Figure 4.7, note the scale is further decreased to highlight differences in values. The numerical solvers predict little to no change between cooling flow pressures when removing the exhaust shield, however the wind tunnel results show larger changes.

It was thought that the difference between the numerical solvers and wind tunnel results for  $\Delta\Delta C_{p_{B-A}}$  could be due to the wind tunnel heating up during successive runs causing a difference in the air density. A short investigation by manually altering the density based on the measured temperatures for each wind tunnel run concluded that the temperature difference alone is not enough to remove the offset between test and simulation. A single reason for the difference in pressures was not found meriting further investigation to determine whether the difference is due to the simulations not capturing the effect or if the effect is an artifact of the wind tunnel tests.

## Engine bay probes

The engine bay probes were also investigated to see how the underhood pressures are predicted by the numerical solvers for open and closed cooling. Based on the results displayed in Figure 4.8, the pressure probe

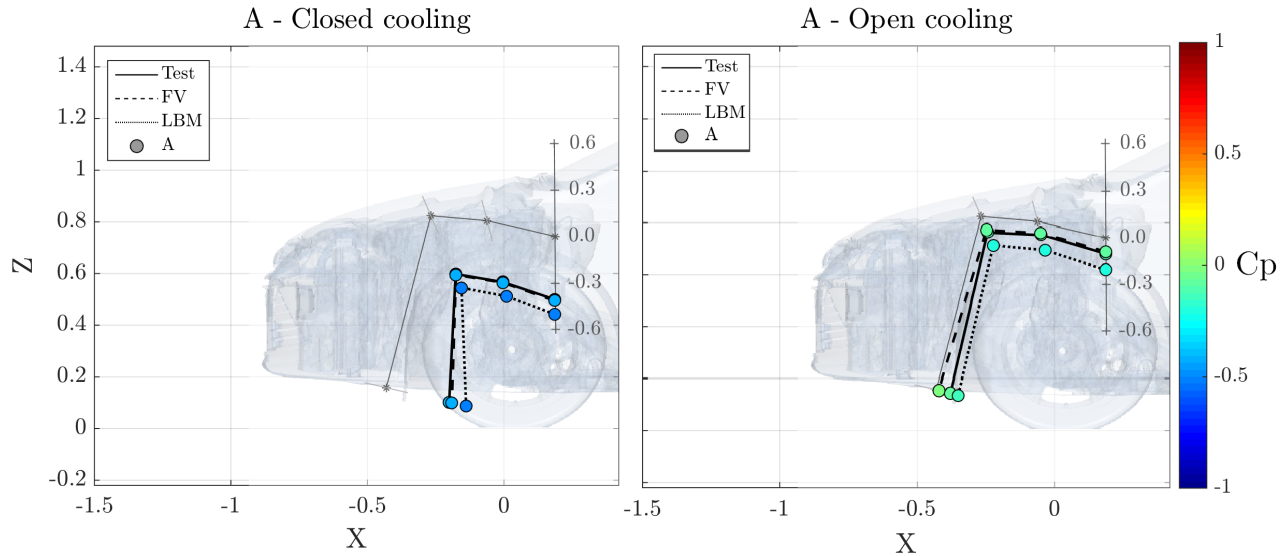


Figure 4.8: Engine bay probe - Configuration A, Open and Closed cooling

measurements for the FVM solver agree better with test results than the LBM solver. However looking at the pressure probe results for the AGS closed operation condition, Figure 4.9, it's not clear which solver is giving better predictions of the underhood pressures. Contrary to the centerline probes, the numerical solvers are now differing showing overpredictions of the engine bay pressures for the FVM solver and underpredictions for the LBM solver. The overpredicted pressures in the engine bay for the FVM simulations could be caused by

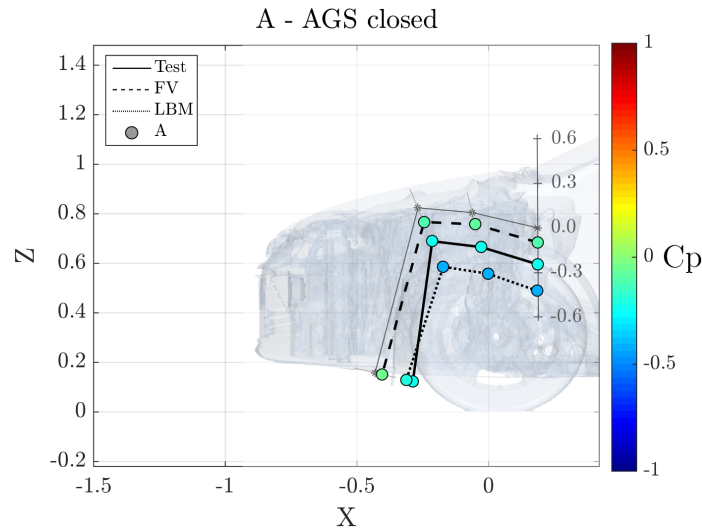


Figure 4.9: Engine bay probe - Configuration A, AGS Closed

the increase in blockage caused by the surface wrapping operation while meshing. The surface wrapper joins geometry of small sizes with close proximity (based on the mesh settings) so that details such as two parallel pipes become one joined and larger body.

## Hood probes

The probes on the hood are plotted as an array with the pressure written in the cells and the colour corresponding to the pressure,  $C_p$ . The hood pressure for open, closed and delta cooling are plotted in Figure 4.10. The pressure predicted at the leading edge by the numerical solvers is lower ( $\sim 0.1C_p$ ) than the wind tunnel results.

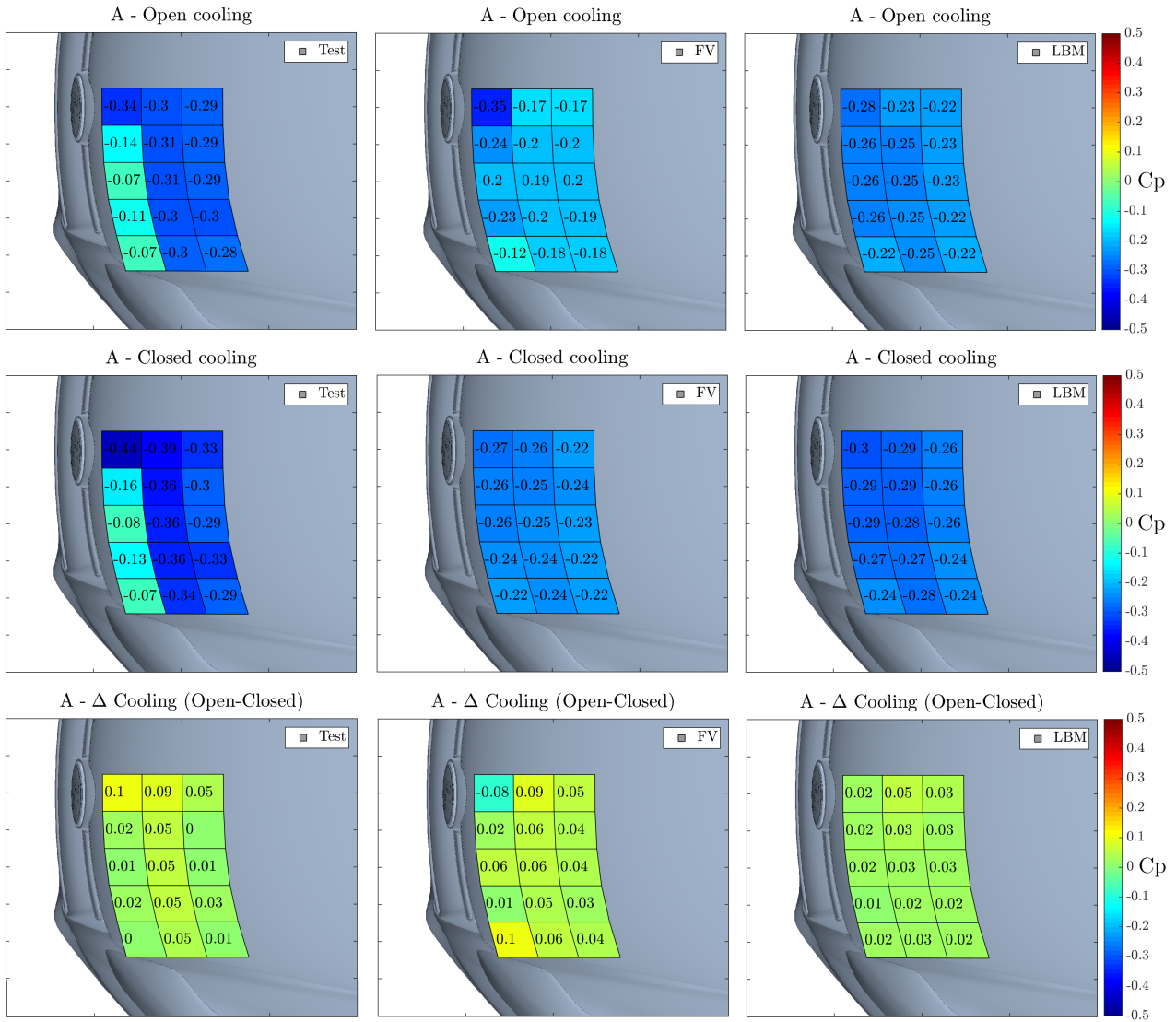


Figure 4.10: Hood probes - Configuration A

In order to highlight the differences in predicted pressures the results are also plotted relative to the wind tunnel tests as shown in Figure 4.11. The difference in pressures due to cooling flow is predicted closer to wind tunnel results than the pressures predicted for either open or closed cooling.

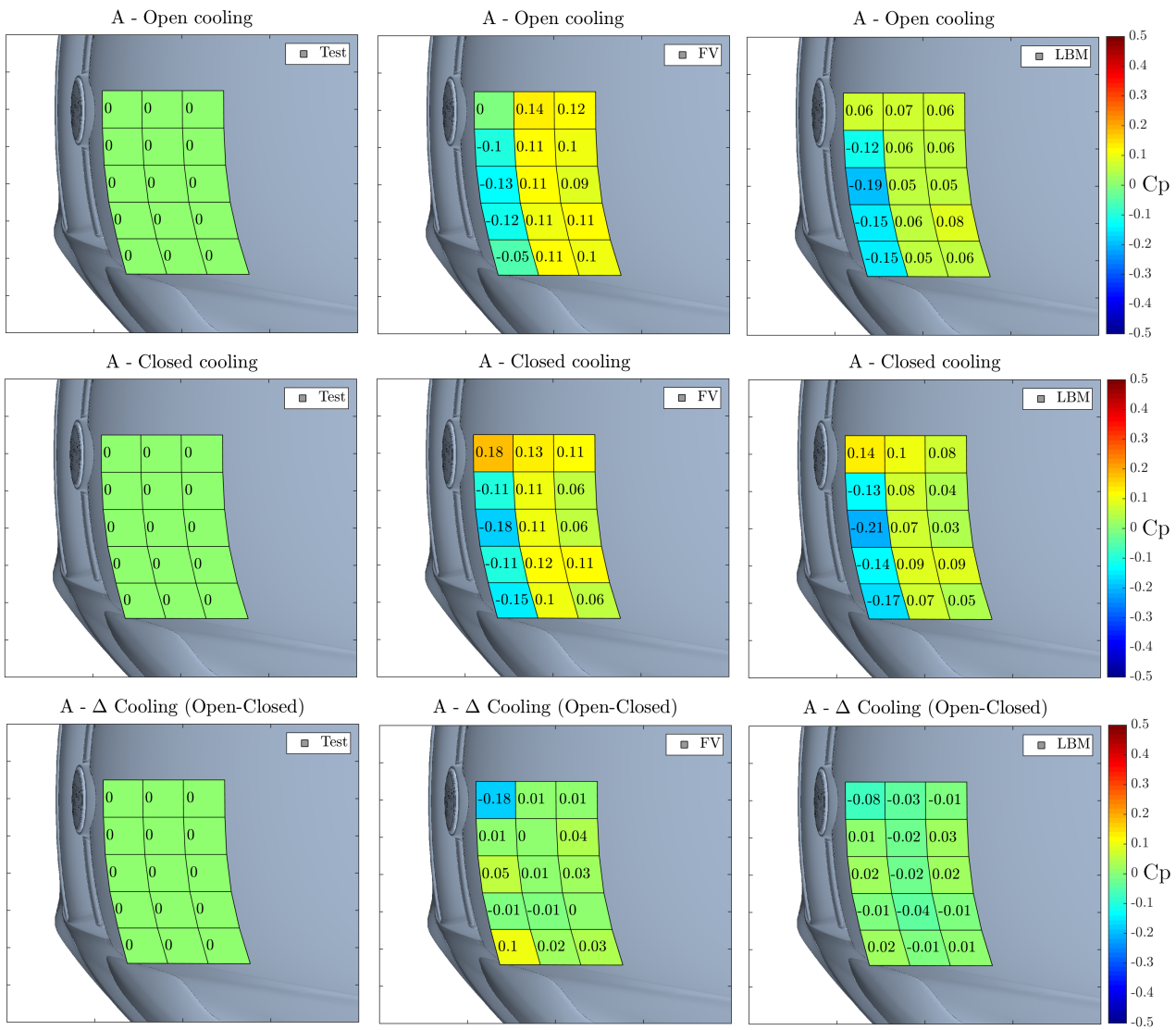


Figure 4.11: Hood probes - Configuration A, Normalized by Wind Tunnel results

## Front bumper probes

The front bumper probes are displayed in the same manor as the hood probes. The wind tunnel tests display a probe of high pressure (0.38) (Figure 4.12) in the second row, second column. The high pressure seen in this region seems unphysical suggesting that the probe in the wind tunnel might have an offset due to calibration issues for example. The difference between open and closed pressure for this probe is however reasonable.

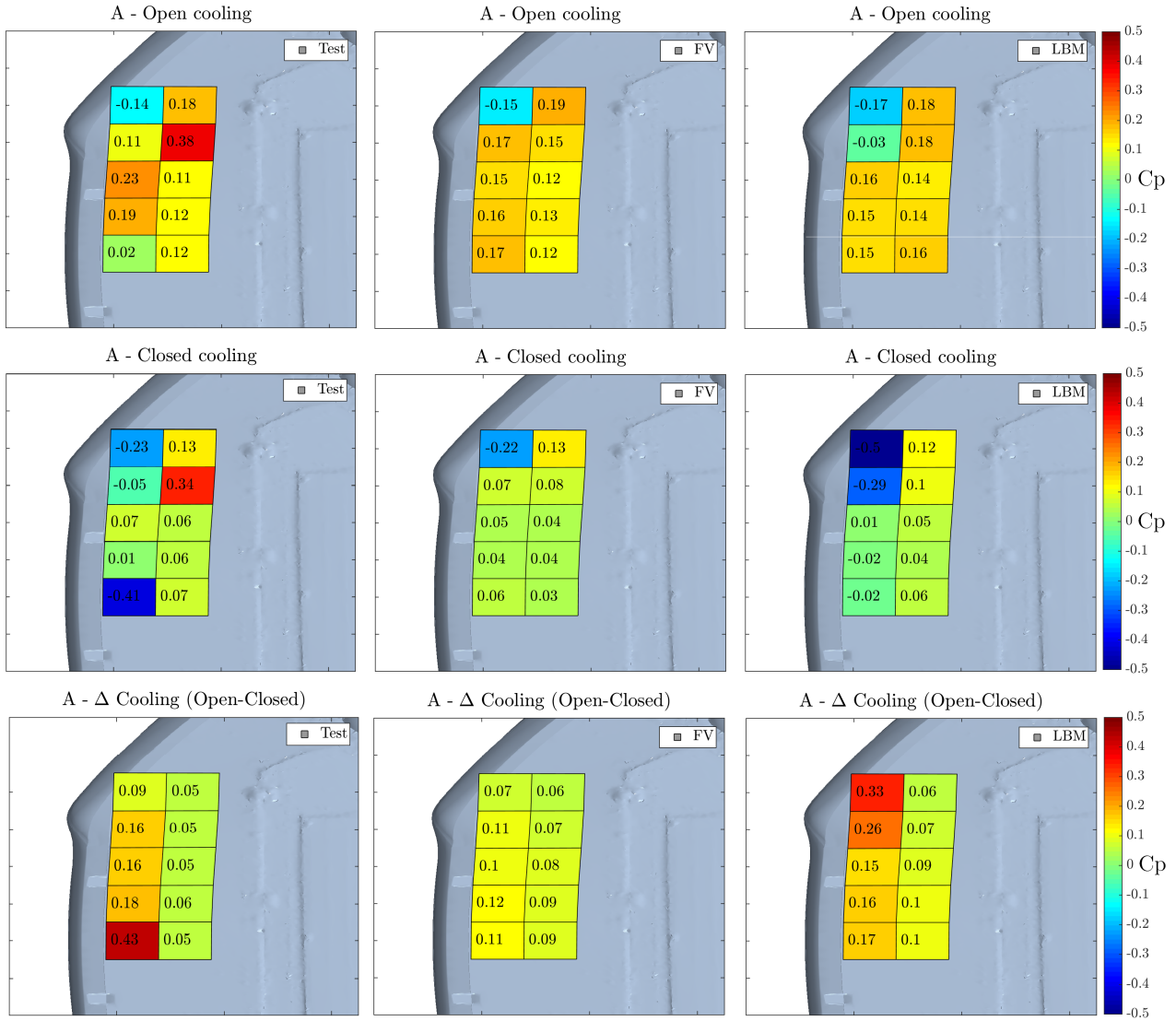


Figure 4.12: Front bumper probes - Configuration A

The low pressure seen in the probe located in the first column, last row for the closed test case has been previously explained for when presenting the centerline probe results as a possible geometrical difference between the real and virtual geometry. Comparing the difference in cooling pressure between the numerical solvers and wind tunnel results, the FVM prediction matches closer to the test results than the LBM solver. However, it should be noted that measuring only a point (probe) can impact the solution significantly when the probe is located in an area of high pressure gradient.

The results for the bumper are also displayed relative to the wind tunnel tests, Figure 4.13. Comparing the relative hood pressures with the bumper pressures Figure 4.11, 4.13, we can see that the hood pressures are on average overpredicted while the front bumper pressures slightly underpredicted. For the open cooling condition the average overprediction on the hood is  $C_{p_{relative,average}} = 0.05$  and the average underprediction on the bumper is  $C_{p_{relative,average}} = -0.01$  giving an average difference of  $C_{p_{average,diff}} = 0.06$ . As shown previously in Table 4.1 an increase of  $C_{p_{increase}} = 0.1$  on the hood can result in fifty counts front lift change.

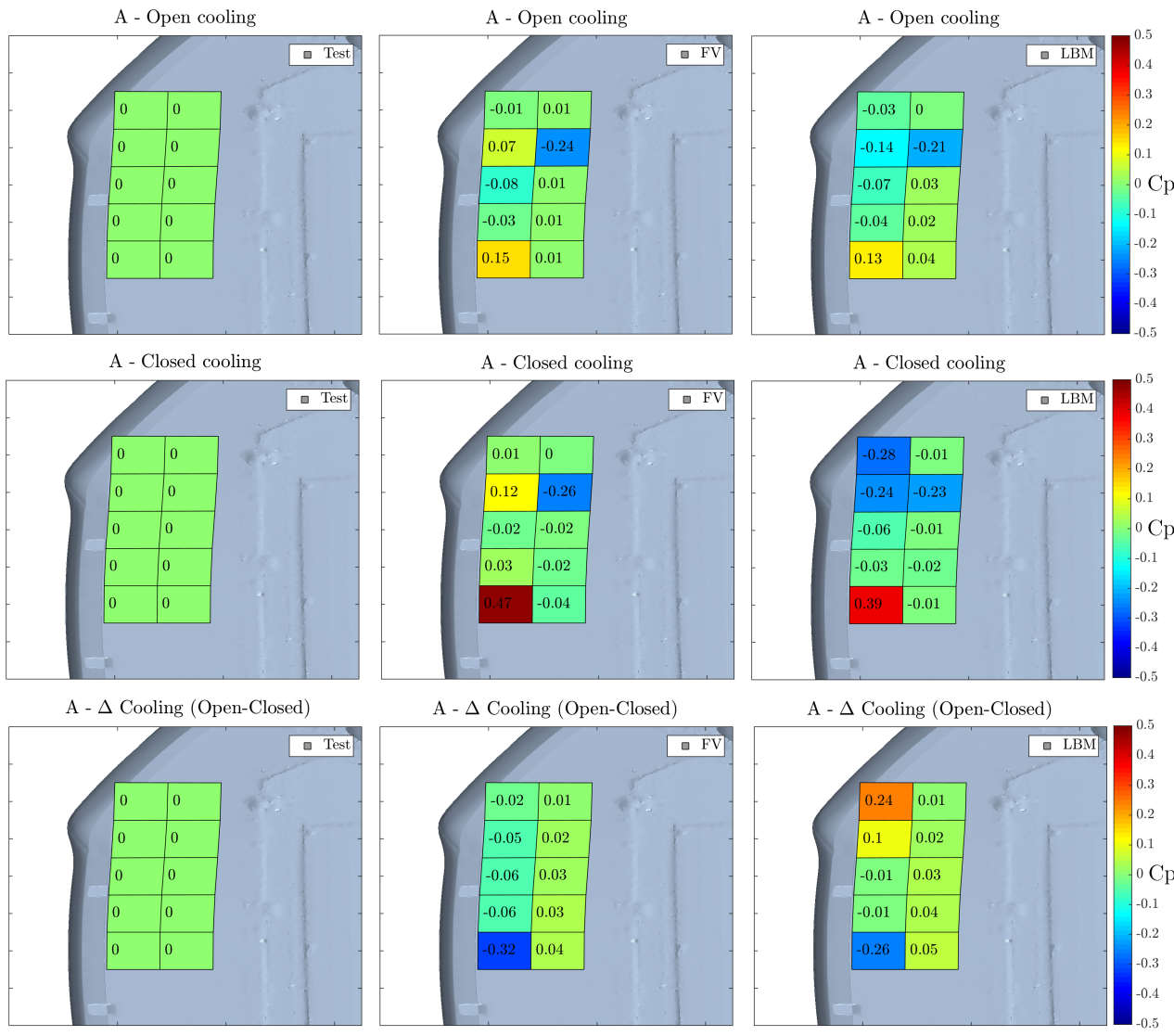


Figure 4.13: Front bumper probes - Configuration A, Normalized by Wind Tunnel results

## 4.2 Front lift and cooling drag interaction

In the background it is mentioned that a possible connection between cooling drag and front lift was observed by Ford Motor Company in the wind tunnel results, as well as a significant offset in front lift between wind tunnel tests and CFD. The interaction between cooling drag and front lift is investigated in this section with the help of the FVM simulations results. The results are post-processed and compared with the help of Accumulated 1D plots, Integrated 2D plots and mass flows through control planes.

### 4.2.1 Accumulated 1D

The Accumulated 1D plots include the open and closed cooling condition as well as the difference between open and closed cooling. Looking at how the cooling drag and cooling front lift is built up along the vehicle we can see from Figure 4.14 that the largest changes happen at the front part of the vehicle with smaller changes in the rear. The same plot but for configuration B, Figure 4.15, reveals differences in the cooling flow forces by

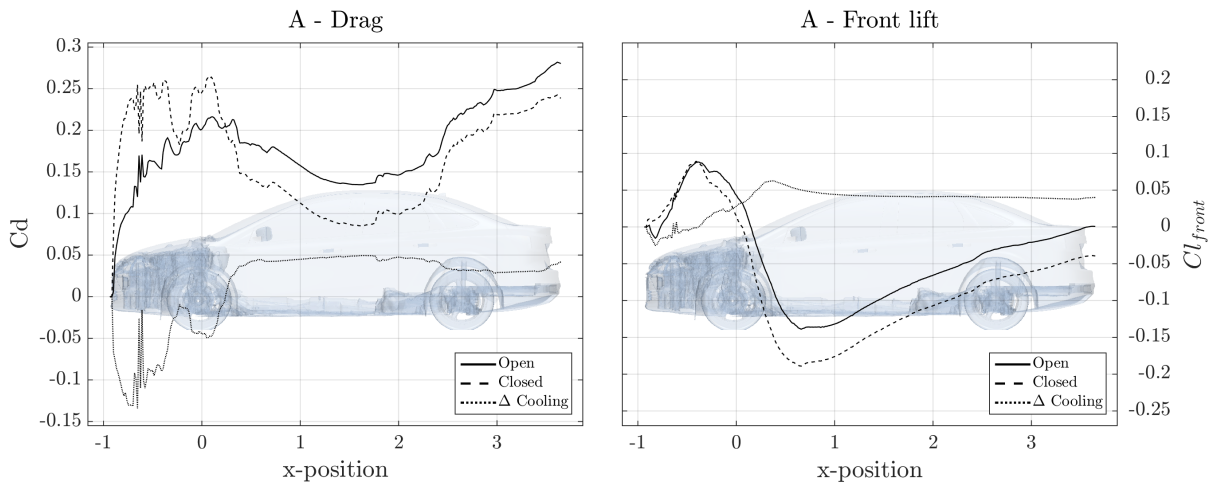


Figure 4.14: Accumulated 1D - Open, Closed and  $\Delta$  cooling for configuration A

removing the exhaust shield. When removing the exhaust shield we see that the cooling drag is increased in the rear part of the car, which is primarily due to the increased drag for configuration B with closed cooling. We can also see an increase in cooling lift for configuration B compared to configuration A in the middle of the car. Looking back at the comparison of drag for the numerical results and wind tunnel test, Figure 4.1a, we saw that the numerical solvers overpredicted drag for closed cooling for configuration B suggesting that the effects seen is exaggerated in the simulations.

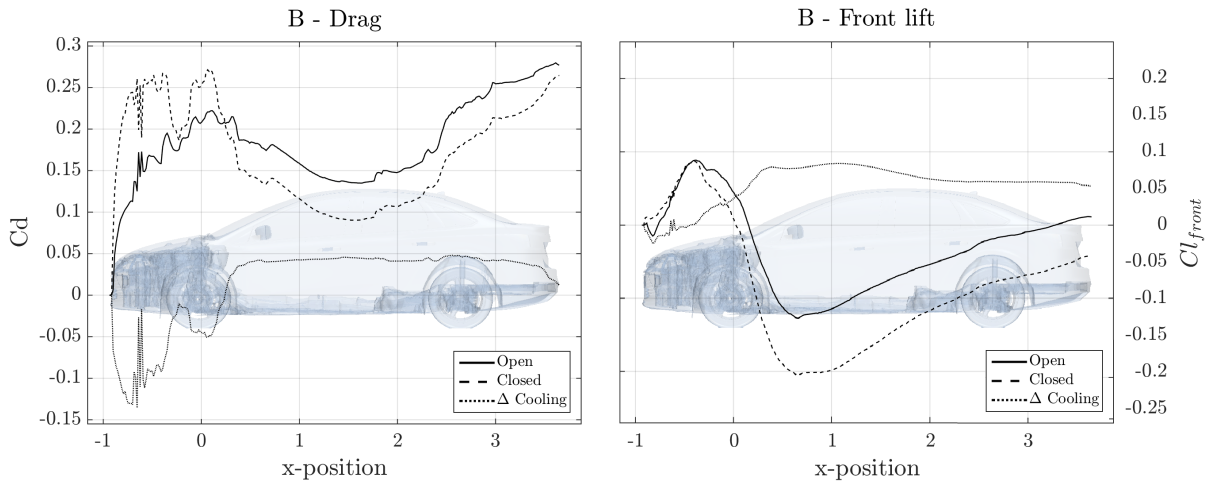


Figure 4.15: Accumulated 1D - Open, Closed and  $\Delta$  cooling for configuration B

## 4.2.2 Integrated 2D

Integrated 2D plots are used to gain further insight in how the forces are distributed over the vehicle and highlight areas of interest. The integrated 2D plots are for example used to highlight changes in cooling drag between vehicles configurations. The 2D integrated plots and how they're generated is explained in the Method chapter, page 15. From Figure 4.16 we can see large differences in drag at the front of the car between the

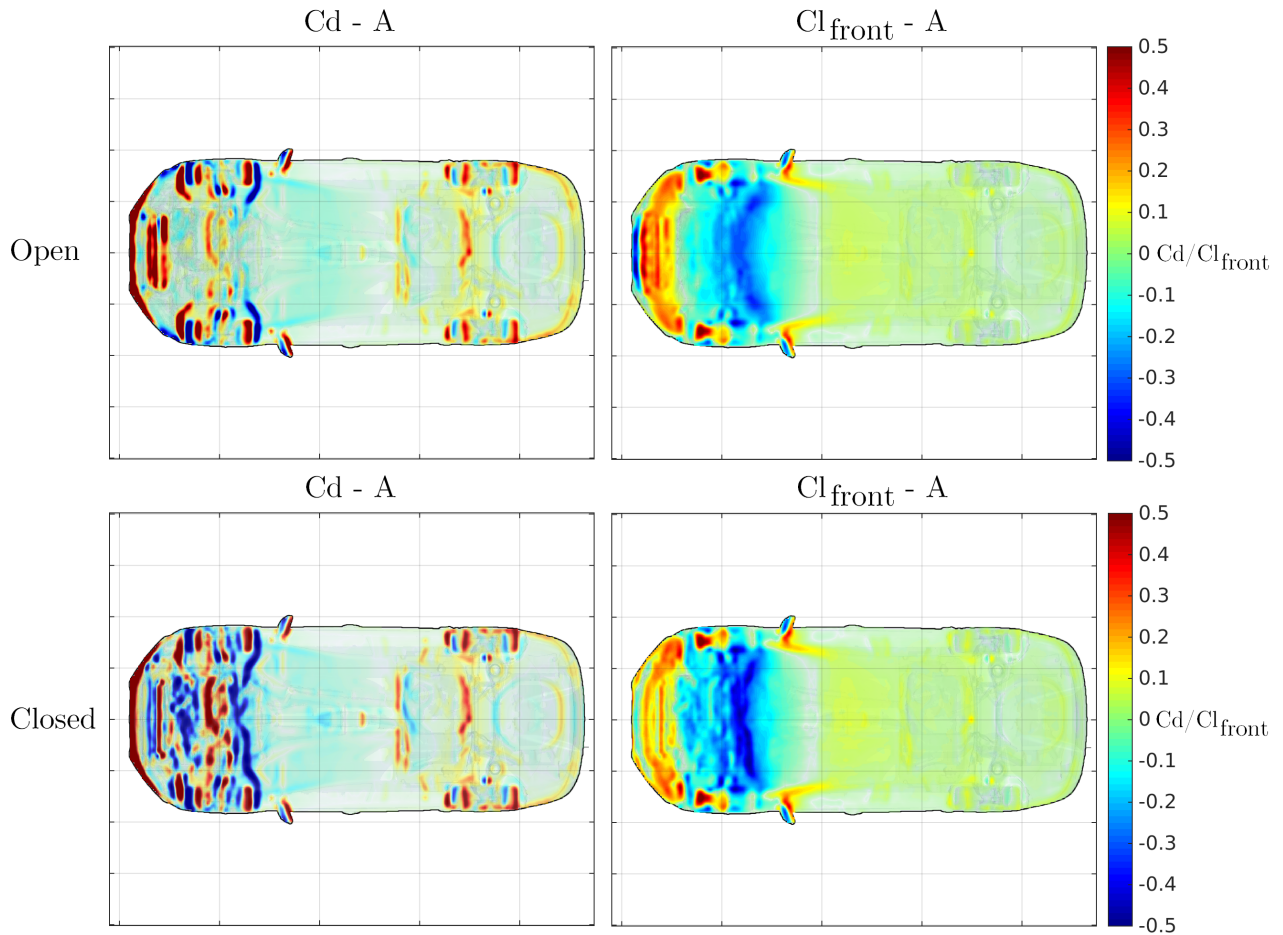


Figure 4.16: *Integrated 2D - Open cooling for configuration A*

open and closed cooling. For front lift the differences are more subtle and hard to distinguish between the open and closed cooling results.

## $\Delta$ Cooling

In order to make it easier to determine how the cooling flow is effecting the system, the difference ( $\Delta$  cooling), is plotted. Looking at the force distribution due to cooling flow, Figure 4.17, we can see that most of the change is located at the front of the car for both drag and lift which could also be seen in the Accumulated 1D plots.

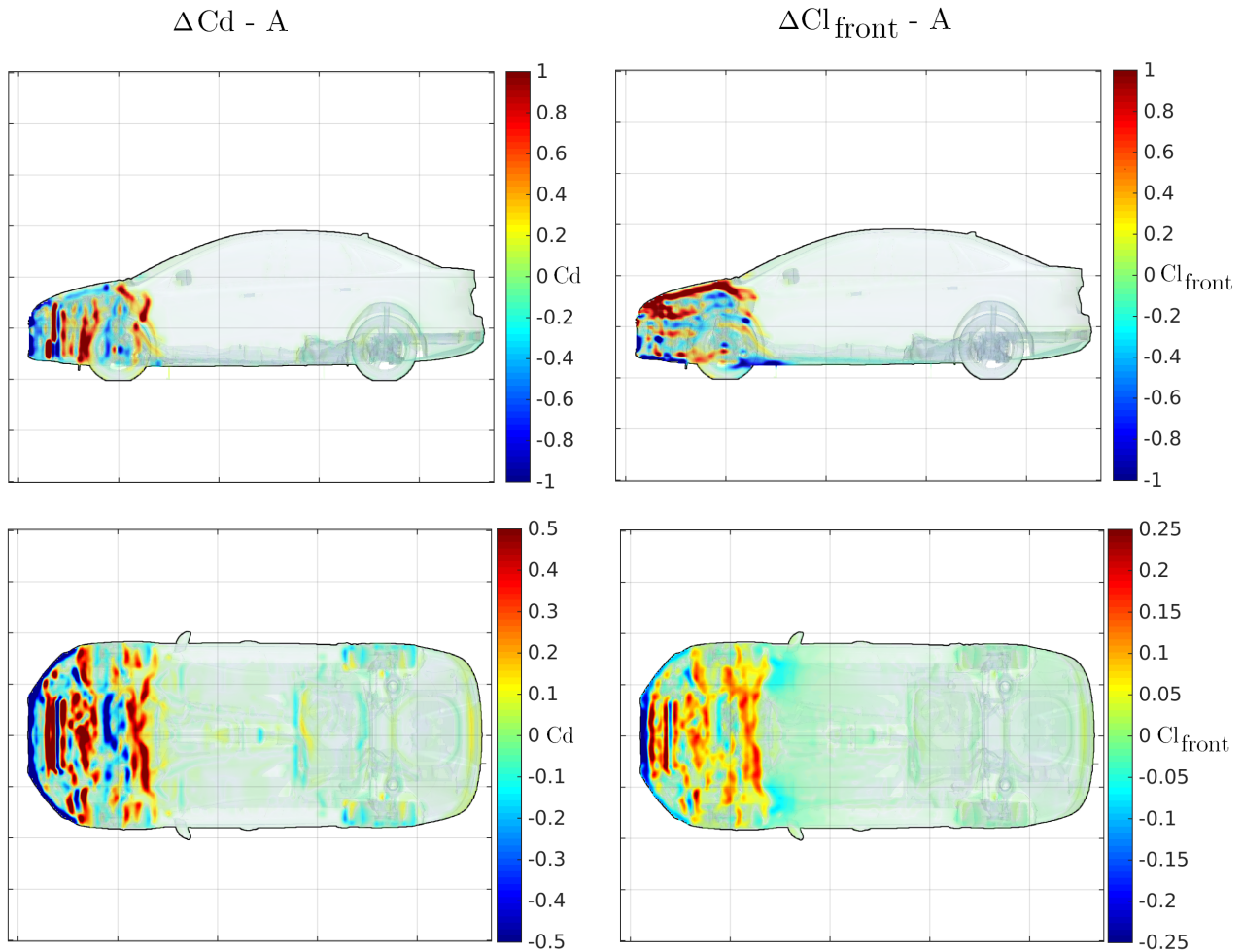


Figure 4.17: *Integrated 2D - Delta cooling for configuration A*

The cooling drag and cooling lift is 42 and 40 counts respectively. Looking closely at the distribution of the cooling lift and cooling drag we can see that the regions of high/low lift and drag coincide when looking at the planform view of the vehicle.

This can be explained by looking at the equation for front lift, Equation 2.4. The front lift is a function of drag, lift and the centre of pressure. By splitting the lift and drag component in Equation 2.4, we can plot the

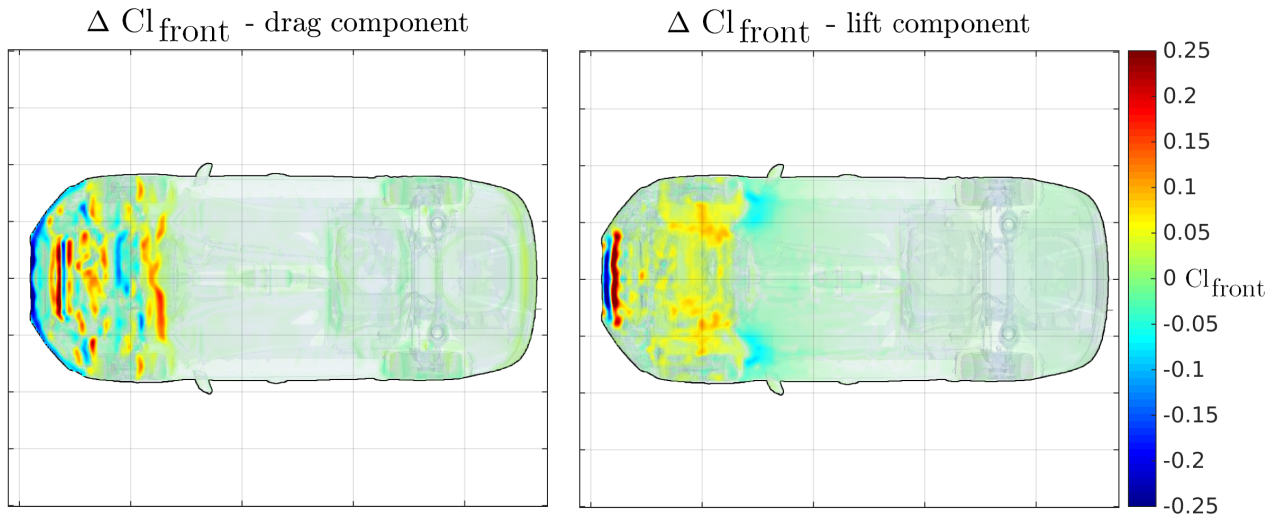


Figure 4.18: *Integrated 2D - Delta front lift of components for configuration A*

contributions of the different components. As shown in Figure 4.18 we can see how the components of drag and lift effects the cooling front lift separately. Comparing the drag component of front lift, Figure 4.18, with the cooling drag, Figure 4.17, we can see which areas of cooling drag have significant impact on front lift.

### $\Delta\Delta$ Cooling difference between configurations

To further investigate how the interaction between cooling front lift and cooling drag is connected, the differences between the configurations is investigated. As shown in the Method chapter, page 10, the difference in cooling flow drag between configuration A and B is written as  $\Delta\Delta Cd_{B-A}$ .  $\Delta\Delta Cd_{B-A}$  can be read as the change in cooling drag when removing the exhaust shield and  $\Delta\Delta Cd_{C-A}$  can be read as the change in cooling drag when removing the engine cover.

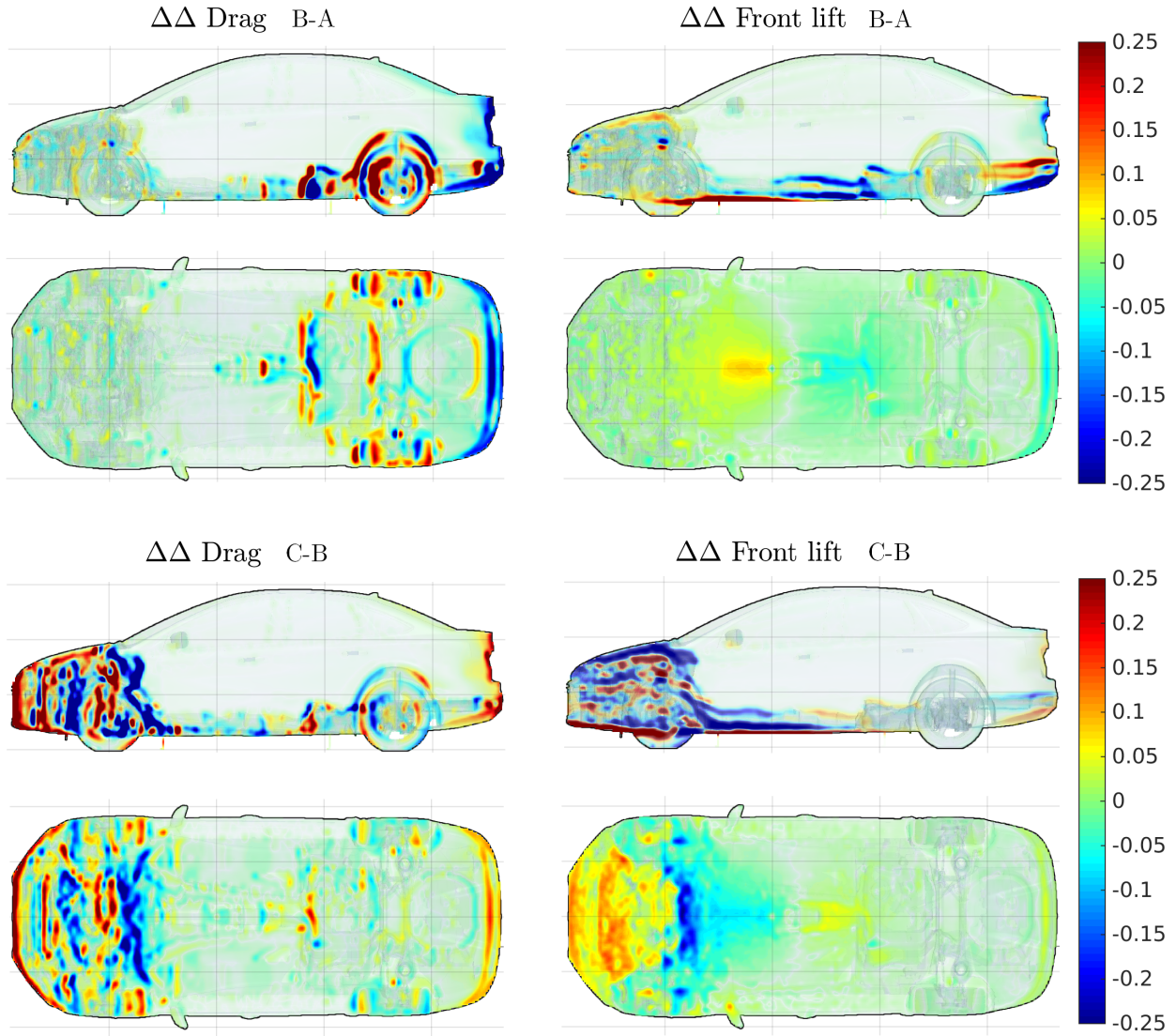


Figure 4.19: *Integrated 2D - Delta delta front lift and drag*

The change in front lift and cooling drag between configurations, shown in Figure 4.19, is not located in the same areas of the vehicle which was seen when comparing the cooling front lift and drag (Figure 4.17). We can also see that the force distribution between configurations can have very different impacts on the force distribution depending on the configuration.

### 4.2.3 Mass flow

The difference in mass flow around the vehicle was also investigated in the simulations to gain understanding in how the flow field is redistributed around the vehicle for opened and closed cooling. The change between open and closed cooling is plotted Figure 4.20. Positive mass flow for the wheel is defined as outboard of the car. The control planes around the car can be seen in the Method chapter, page 16. The mass flow change through the rims due to cooling flow is effected differently depending on the configuration where we can see an increase in mass flow through the front wheels when removing the engine shield for example. Comparing the difference in mass flow for the rear wheels of configuration A and B we see a change in the direction of mass flow. Looking back at the results for  $\Delta\Delta Cd_{B-A}$ , Figure 4.19, we saw changes in drag around the rear wheels suggesting that the mass flow through the rear wheels could be an influencing factor on the cooling drag change between configuration A and B. However the connection between the cooling drag increase when removing the exhaust shield and the mass flow through the rear wheels needs further investigation.

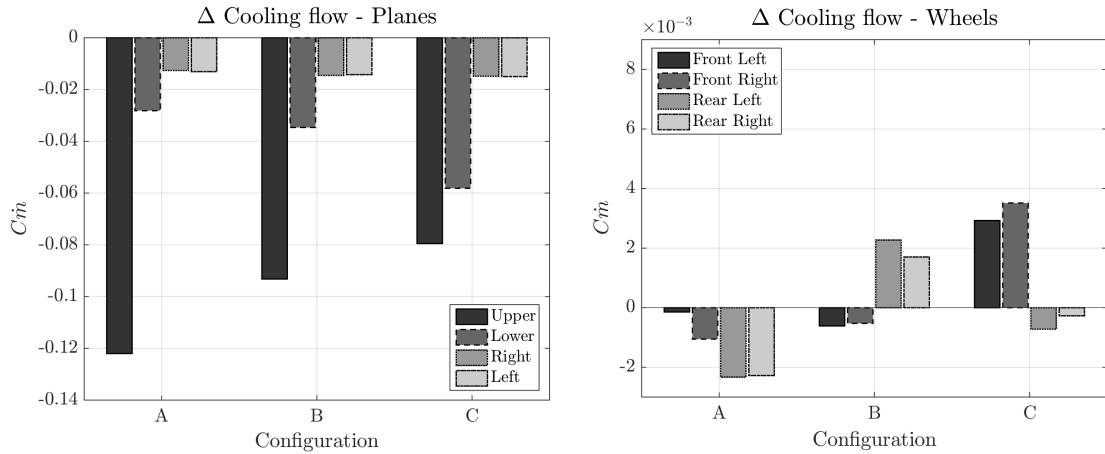


Figure 4.20: Cooling mass flow change - Rims and Control planes

A reduction in mass flow around the vehicle is seen when opening the cooling is observed where the mass flow around the sides of the vehicles is not effected as much as above and below the vehicle. The different configurations has a small impact on the mass flow reduction to the side of the vehicle. The mass flow above and below the vehicle however shows a larger impact between configurations.

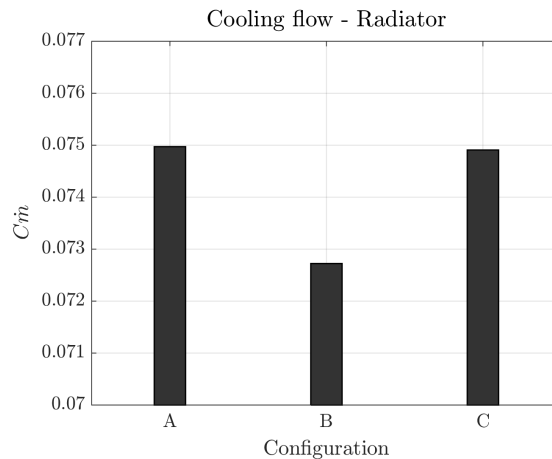


Figure 4.21: Cooling mass - Radiator

The radiator mass flow, Figure 4.21, show similar mass flows for configuration A and C with a reduction of  $\sim 2.5\%$  for configuration B. It should be noted that the combined reduction in mass flow around the vehicle does not equate to the increase through the radiator. This is due to that the control planes do not form a tight seal around the car body and that the radiator is not sealed tight to the grille.

## 5 Discussion

The discussions is oriented around the results and recommendations for future work. Potential factors influencing the results between the CFD and wind tunnel test are also discussed.

### 5.1 Results

The numerical accuracy and trend predicting capability for the two numerical solvers is similar for the setup used in the thesis work. The absolute front lift is underpredicted by  $\sim 60 - 70$  counts by both numerical solvers, with the magnitude of front lift due to cooling flow predicted within  $\sim 15$  counts. The trend predicted for front lift and drag between configurations is not improved with the FVM solver over the LBM solver. Even significant changes such as removing the engine cover is not predicted well with the numerical solvers. The numerical solvers are often close in predictions, however looking at for instance the probe array under the front bumper, Figure 4.12, there are significant differences in the predicted probe pressures between the solvers. The planform area of the vehicle is  $\sim 3.4$  times larger than the frontal area which can however exaggerate errors in lift compared to drag when looking at absolute drag and lift values.

### 5.2 Influencing factors

Potential factors that cause differences between the numerical results and wind tunnel results is discussed in this section.

#### 5.2.1 Wind tunnel

The centerline pressure probe results showed an offset between the numerical and wind tunnel results which is to be expected since the wind tunnel geometry is not modelled. However, it can not be determined if the offset seen in the results is only due to the geometrical differences between experiment and simulation and merits further investigation. Another factor related to the wind tunnel geometry that could influence the results is the wind speed in the virtual and experimental wind tunnel. In the simulations the wind speed is set as a uniform velocity across the entire inlet while in the real wind tunnel a nozzle is used to increase the velocity of the fluid before reaching the test section. Depending on how the velocity is measured in the wind tunnel there might be an offset in wind speed between the experiment and simulation which could further influence the pressure probe offset seen between the experiments and simulations.

Additionally when looking at the 2D probe arrays on the lower bumper and hood we can see an overprediction of pressure on the hood and an underprediction on the lower bumper compared to wind tunnel tests. The cause of the pressure difference is unknown, however the pressure difference reduces front lift compared to experiments.

### 5.2.2 Probe location

The probe location can have a significant impact when comparing the wind tunnel tests with the simulation results. As can be seen below in Figure 5.1 the surface pressure gradient is large near the leading edge of the hood making the results sensitive to probe location.

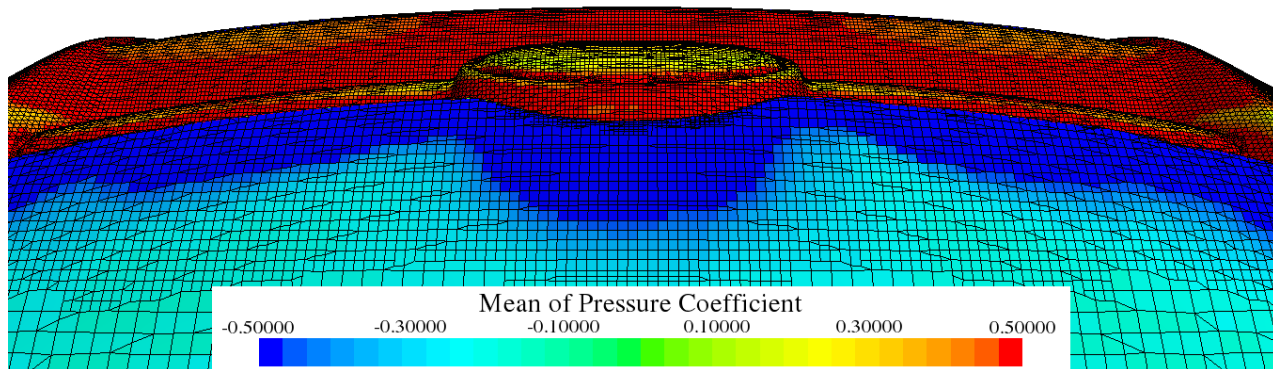


Figure 5.1: *Hood pressure and mesh*

### 5.2.3 Geometry

There exist geometrical differences between the virtual and real vehicle that could influence the results. For example there is geometrical differences between the cooling blanking used in the wind tunnel and CFD as seen in Figure 5.2. The blanking used in the real wind tunnel is taped on and under aerodynamic loads will deform compared to the smooth surface used for blanking in the numerical simulations.



Figure 5.2: *Closed cooling - Virtual vs real*

The tyres used in CFD are slick with three rain grooves and cut at the ground. Tyre features such as cut tyres, rain grooves and the tread can have a significant impact on lift. By adding rain grooves Hobeika [23] found that the lift was increased if the tyre was cut and decrease if the tyre was deformed to allow flow through the rain grooves.

## 5.3 Future work

Suggestions on future work is given in this section. The suggestions given are sorted by investigations into numerical accuracy and further investigation into front lift and cooling flow.

### 5.3.1 Numerical accuracy

The numerical accuracy for the FVM simulations compared to the LBM simulations offered no increase (or decrease) in accuracy and trend predicting capability based on the nine simulations run for this thesis work. Note that this should not be taken as an indication of the predictive capability for either the FV or LB-method as a whole. The thesis work done was limited in time and also limited in computational cost for time constraints as well as keeping the comparison between the two solvers fair. Based on the inconsistent capability to capture the trends it is suggested to investigate improvements in the simulation setup. Incorporating the geometry of the wind tunnel, adjusting the geometry of the cooling blanking, increasing the mesh resolution and using sliding mesh for rim rotation are examples of areas that can be interesting to investigate the importance of.

Improving the numerical setup and validating that improvement is however not trivial and easy. Looking at just drag and lift for example can lead to error cancellation where the flow field predicted is wrong but giving good drag and lift predictions for a given vehicle. Ideally the setup improvement would be done and validated for several vehicle types, configurations for both open and closed cooling.

### Geometry

Reducing the uncertainty of geometrical differences between the real and virtual vehicle is another area of interest that can be investigated. There has already been work done to the vehicle used in the wind tunnel, for example the gaps on the bodywork has been taped as seen in Figure 5.2. Reducing the uncertainty in geometrical representation could of course be taken further, for example small details such as wires could be replaced by fully rigid and well known geometry or removed entirely. The idea is however not to simplify the geometry to such extent that it is no longer representative of a production vehicle, it is only to reduce the uncertainty in the geometry.

### Wind tunnel test

By using results from four simulations the difference in cooling flow between configurations was investigated. It was however found that the trends predicted by the FVM simulations between configurations were not consistently predicted and differed from wind tunnel results. To investigate where the difference occur it would be interesting to first run CFD simulations to identify areas where the cooling flow has changed and then do wind tunnel tests with pressure probes placed in these key areas. By running the CFD simulations before the wind tunnel test we can place measurement tools in areas of interest in the wind tunnel and determine how the for example pressures are under/overpredicted by CFD in these areas.

### 5.3.2 Front lift and cooling flow interaction

The work performed in this thesis has identified areas of interest and looked at how drag and front lift due to cooling flow are connected and distributed. Further investigations with focus on the flow and how the flow is increasing the front lift when opening the cooling is recommended to give insight into how to design a vehicle with a low front lift increase due to cooling flow.

### Integrated 2D plots

The Integrated 2D plots shown in this thesis contain information of both the external and internal surface forces. Splitting the plot by external and internal surfaces can help determine key areas of interest faster so that more elaborate post processing can be focused on these areas.

## 6 Conclusions

One area of interest stated in the purpose of the thesis was to investigate and compare the accuracy and predictive capability of FVM and LBM simulations to wind tunnel tests. The two numerical solvers have similar predictive capability based on the nine simulations run in this thesis work. Worth noting is that the solvers accuracy and trend predicting capability was similar for the *specific* simulation setup used in this thesis and should not be read as an indication of the predictive capability for either the FV or LB-method as a whole. It is also evident from the results that the two numerical solvers are often closer to each other than to the wind tunnel results.

The second area of interest in the thesis is the interaction between front lift and cooling drag. As can be seen in Figure 4.17 the areas of high and low cooling drag largely coincide with the areas of high and low cooling front lift. There is a clear interaction which can be explained by looking at how the front and rear lift balance is effected by drag, equation 2.4. From equation 2.4 we see that the front lift,  $Cl_{front}$ , is linearly dependent on the drag force,  $Cd$ , and the moment arm,  $Z$ , acting on that force. While there is a clear interaction between cooling drag and front lift the changes in cooling front lift and cooling drag between configurations are impacted significantly different as can be seen in Figure, 4.19.

## References

- [1] J. Howell and G. L. Good. The Influence of Aerodynamic Lift on High Speed Stability. *International Congress and Exposition Detroit, Michigan March 1-4, 1999* (1999).
- [2] S. Koitrاند et al. A Computational Investigation of Ground Simulation for a Saloon Car. *SAE International Journal* (2014). DOI: 10.4271/2014-01-0615.
- [3] O. Fischer et al. CFD Approach to Evaluate Wind-Tunnel and Model Setup Effects on Aerodynamic Drag and Lift for Detailed Vehicles. *SAE International Journal* (2010). DOI: 10.4271/2010-01-0760.
- [4] A. Kremheller. The Aerodynamics Development of the New Nissan Qashqai. *SAE Technical Paper* (2014). DOI: 10.4271/2014-01-0572.
- [5] T. Kuthada and J. Wiedemann. Investigations in a Cooling Air Flow System under the Influence of Road Simulation. *2008 World Congress Detroit, Michigan April 14-17, 2008* (2008).
- [6] S. Noelting and E. Fares. The Lattice-Boltzmann Method: An Alternative to LES for Complex Aerodynamic and Aeroacoustic Simulations in the Aerospace Industry. *SAE International Journal* (2015). DOI: 10.4271/2015-01-2575.
- [7] H. Versteeg and W. Malalasekera. *An Introduction to Computational Fluid Dynamics: The Finite Volume Method (2nd Edition)*. Pearson, 2007. ISBN: 0-131-27498-8.
- [8] G. K. Batchelor. *An Introduction to Fluid Dynamics*. Cambridge University Press, 2010. ISBN: 9780511800955.
- [9] P. Moin and K. Mahesh. DIRECT NUMERICAL SIMULATION: A Tool in Turbulence Research. *Annual Review of Fluid Mechanics* (1998). DOI: 10.1146/annurev.fluid.30.1.539.
- [10] L. Davidson. DIRECT NUMERICAL SIMULATION: A Tool in Turbulence Research (2015). URL: [http://www.tfd.chalmers.se/~lada/postscript\\_files/solids-and-fluids\\_turbulent-flow\\_turbulence-modelling.pdf](http://www.tfd.chalmers.se/~lada/postscript_files/solids-and-fluids_turbulent-flow_turbulence-modelling.pdf).
- [11] F. Billard. DEVELOPMENT OF A ROBUST ELLIPTIC-BLENDING TURBULENCE MODEL FOR NEAR WALL, SEPARATED AND BUOYANT FLOWS. *Doctor of Philosophy* (2011).
- [12] L. Davidson. Large Eddy Simulations: how to evaluate resolution. *Int. J. of Heat and Fluid Flow* (2009).
- [13] P. Spalart. The 2007 Hybrid RANS-LES Symposium: An Outsider's View. *Symposium of Hybrid RANS-LES Methods, Corfu, Greece* (2007).
- [14] M. F. R. and K. M. Adaptation of Eddy-Viscosity Turbulence Models to Unsteady Separated Flow Behind Vehicles. *Engineering Conferences International: The Aerodynamics of Heavy Vehicles: Trucks, Buses and Trains* (2002).
- [15] S. M. L.-S. M. K. Travin A. and P. R. Spalart. PHYSICAL AND NUMERICAL UPGRADES IN THE DETACHED-EDDY SIMULATION OF COMPLEX TURBULENT FLOWS. *Advances in LES of Complex Flows, R. Friedrich and W. Rodi Eds., Kluwer Academic Press, pp. 239-254* (2002).
- [16] C. Adapco. STAR-CCM+ User guide (2016). URL: [https://stevedocs.cd-adapco.com/starccmplus\\_latest\\_en/index.html](https://stevedocs.cd-adapco.com/starccmplus_latest_en/index.html).
- [17] M. K. S. A. K. T. M. L. Shur P. R. Spalart. A hybrid RANS-LES approach with delayed-DES and wall-modelled LES capabilities. *International Journal of Heat and Fluid Flow* (2008).
- [18] C. Adapco. STAR-CCM+ (2012). URL: [http://www.cd-adapco.com/sites/default/files/Presentation/Heat-Transfer-Best-Practices-Nov2012\\_PE.pdf](http://www.cd-adapco.com/sites/default/files/Presentation/Heat-Transfer-Best-Practices-Nov2012_PE.pdf).
- [19] P. W. tunnel. Turin, Italy (2016). URL: [http://www.pininfarina.se/en/services/wind\\_tunnel](http://www.pininfarina.se/en/services/wind_tunnel).
- [20] C. Adapco. STAR-CCM+ (2016). URL: <http://www.cd-adapco.com/products/star-ccm>.
- [21] C. Adapco. STAR-CCM+ (2012). URL: <http://www.cd-adapco.com/presentation/best-practices-workshop-ii-volume-meshing>.
- [22] S. R. A. G. Sofie Koitrاند Lennart Lofdahl. A Computational Investigation of Ground Simulation for a Saloon Car. *2014 SAE International* (2014).
- [23] T. Hobeika. Investigation of Tyre Geomtry Influence on Road Vehicle Aerodynamics. *Chalmers Masters Thesis* (2012).